Volume 7, Issue 8, 2025

Print ISSN: 2663-1938
Online ISSN: 2663-1946

JOURNAL OF COMPUTER SCIENCE AND ELECTRICAL ENGINEERING

Journal of Computer Science and Electrical Engineering

Volume 7, Issue 8, 2025

Published by Upubscience Publisher

Journal of Computer Science and Electrical Engineering
Print ISSN: 2663-1938 Online ISSN: 2663-1946
Email: info@upubscience.com
Website: http://www.upubscience.com/

Table of Content

Journal of Computer Science and Electrical Engineering
Print ISSN: 2663-1938
Online ISSN: 2663-1946
DOI: https://doi.org/10.61784/jcsee3105

GRAPH-RAG ENHANCED RETRIEVAL AND MULTI-AGENT COLLABORATIVE METHOD FOR INTELLIGENT NUCLEAR POWER ELECTRICAL DESIGN

Yuan Zhang*, YanKun Li, Chao Si
Electrical Department, China Institute of Atomic Energy, Beijing 102400, China.
**Corresponding Author: Yuan Zhang*

Abstract: The design of nuclear power plant electrical systems is characterized by an extensive and intricate body of standards, strong cross-disciplinary coupling, and stringent safety and compliance requirements. Traditional digital design workflows face significant limitations in knowledge reuse, intelligent decision support, and quality assurance. At the same time, general-purpose large language models (LLMs) exhibit hallucinations and lack reliability in safety-critical engineering domains. To address these challenges, this paper proposes an intelligent nuclear power electrical design methodology that integrates knowledge-graph-enhanced retrieval-augmented generation (Graph-RAG) with a multi-agent system (MAS).

First, a domain ontology covering IEC/GB standards, equipment parameter libraries, and design rules is constructed to provide a structured knowledge backbone. Second, a graph-guided hybrid retrieval strategy that combines semantic retrieval with graph path reasoning is designed to enhance retrieval accuracy and contextual relevance. Third, a multi-agent collaboration architecture—comprising requirement analysis, intelligent recommendation, automatic document generation, consistency checking, format review, and interactive question answering agents—is developed. Task orchestration is implemented through a directed acyclic graph (DAG), enabling parallel and coordinated execution of complex design workflows.

Theoretical analysis and scenario-based validation indicate that the proposed approach substantially reduces hallucination rates, improves design efficiency, and ensures the standard compliance of design outputs. Each design decision becomes traceable to explicit standard clauses and equipment parameters, demonstrating the feasibility of the method for the intelligent transformation of nuclear power electrical design and its potential transferability to other complex engineering systems.

Keywords: Nuclear power electrical design; Knowledge graph; Retrieval-augmented generation; Multi-agent systems; Intelligent engineering

1 INTRODUCTION

1.1 Research Background

Nuclear power plant electrical systems constitute a critical component of the overall safety architecture of a nuclear power station. Their design quality directly affects defense-in-depth capability, operational reliability, and controllability under abnormal and accident conditions. With the continuous expansion of nuclear power construction in China, the complexity of safety-related system design has significantly increased. The depth of specialization, knowledge density, and cross-disciplinary coupling in nuclear electrical design far exceed those of conventional industrial power engineering.

According to recent industry statistics, by the end of 2024 China had 55 nuclear power units in operation, and the number of units under construction had ranked first in the world for many consecutive years. The deployment of third-generation reactor technologies such as Hualong One, CAP1400, and EPR has further enlarged the design space, increased equipment parameter complexity, and made technical standards more fine-grained and strongly interconnected across disciplines.

In current practice, nuclear power electrical design still relies heavily on manual consultation of standards, ad hoc retrieval of historical design documents, and item-by-item engineering calculations and compliance checks. Given the extremely stringent safety and regulatory requirements of nuclear power projects, any design deviation may propagate into major risks during subsequent construction and operation stages. Design documentation must therefore be traceable, internally consistent, and highly accurate.

In parallel, the Chinese government has launched an "AI+" national strategy, explicitly calling for the deep integration of advanced AI technologies—including large models—into key industries such as energy, power, and nuclear power. Policy documents such as the *AI+ Energy Implementation Guidelines* emphasize the use of AI models throughout the lifecycle of nuclear power design, manufacturing, and construction, and advocate the development of intelligent nuclear power plants. This provides an unprecedented opportunity for the intelligent upgrading of nuclear electrical design.

However, intelligent nuclear electrical design is far from a simple matter of applying general-purpose LLMs to domain-specific tasks. While LLMs perform well on general language understanding and open-domain question answering,

their applicability in high-safety, highly regulated, and highly complex scenarios such as nuclear power is severely limited, especially in terms of controllability, traceability, and compliance [1].

1.2 Key Challenges in Nuclear Power Electrical Design

Nuclear power electrical design is a prototypical knowledge-intensive engineering activity. Its complexity is reflected in multiple dimensions:

1.2.1 Extensive standards and complex constraints

Nuclear electrical design must simultaneously comply with international standards (IEC series), national standards (GB series), industry standards (NB/DL series), and nuclear safety regulations (HAF series). A single nuclear project involves a large number of mandatory and recommended standards, each containing numerous clauses. These clauses define intricate constraint relationships involving equipment types, safety classes, environmental conditions, EMC requirements, test conditions, and documentation rules.

1.2.2 Difficult knowledge reuse and long experience transfer cycles

Nuclear electrical design is highly dependent on engineers' domain expertise and accumulated project experience. It typically takes many years of training before an engineer can independently undertake nuclear electrical design tasks. This apprenticeship-based knowledge transfer leads to low efficiency, high dependence on key individuals, and difficulty in systematically reusing design knowledge across projects.

1.2.3 Limited applicability of general-purpose LLMs in specialized domains

Studies have shown that general-purpose LLMs exhibit a relatively high factual error rate in specialized engineering tasks and often generate hallucinations. In the nuclear domain, directly querying an LLM about standards may result in non-existent standard identifiers, incorrect clause references, or misinterpretation of technical requirements, which is unacceptable in safety-critical design.

1.3 Related Work

1.3.1 Retrieval-Augmented Generation (RAG)

Lewis et al. proposed retrieval-augmented generation (RAG), which integrates external knowledge retrieval into the generation process and has proven effective for knowledge-intensive natural language processing tasks [2]. Subsequent surveys and extensions have systematically analyzed RAG architectures and demonstrated their ability to mitigate hallucinations and improve factuality in large language models [3].

1.3.2 Knowledge graphs and semantic retrieval

Knowledge graphs provide structured representations of entities and relations, enabling more precise retrieval and logical reasoning over standards, technical manuals, and historical cases. Recent work on graph retrieval-augmented generation (Graph-RAG) shows that incorporating graph-based reasoning into RAG pipelines significantly enhances retrieval accuracy and multi-hop reasoning capability [4].

1.3.3 Multi-Agent Systems (MAS)

LLM-based multi-agent systems decompose complex tasks into collaborative workflows executed by specialized agents. Recent surveys highlight the potential of MAS in workflow orchestration, infrastructure design, and complex task execution, while also pointing out challenges in stability, communication, and governance [5]. Buehler, for example, combines ontologic graphs, RAG, and multi-agent strategies for interpretable materials design, illustrating the value of integrating knowledge graphs, retrieval, and agent collaboration in engineering design pipelines [6].

1.3.4 AI applications in nuclear engineering

Comprehensive reviews indicate that AI has been increasingly applied to reactor analysis, fault diagnosis, safety assessment, and other nuclear engineering areas, and underscore the importance of interpretability and safety in such applications [7]. Domain-specific knowledge graphs have also been used to design safety review decision-support systems for nuclear power plants [8].

These advances collectively motivate the integration of knowledge-graph-enhanced RAG with MAS for nuclear electrical design.

1.4 Research Objectives and Main Contributions

The central objective of this study is to construct an intelligent nuclear power electrical design methodology that integrates domain knowledge, logical reasoning, and parallel collaboration, thereby enabling end-to-end automation from requirement analysis and scheme generation to document delivery.

The main contributions of this work are as follows:

1. **Domain knowledge graph construction:** We propose a knowledge graph construction method tailored to the nuclear electrical domain and build a knowledge backbone covering standards, equipment parameters, and design rules.
2. **Graph-RAG architecture:** We design a graph-guided hybrid retrieval-augmented generation (Graph-RAG) architecture that combines the statistical matching capability of traditional RAG with the logical reasoning capability of knowledge graphs, improving retrieval accuracy and generation quality.
3. **Task-driven multi-agent collaborative design system:** We construct a task-driven multi-agent system (MAS) and implement DAG-based task decomposition and dynamic scheduling, enabling parallel and coordinated execution of complex design workflows.

4. **Method validation in typical engineering scenarios:** We validate the proposed method using representative nuclear electrical design scenarios and demonstrate its advantages in knowledge reliability, design traceability, collaboration efficiency, and quality assurance.

2 INTELLIGENT NUCLEAR ELECTRICAL DESIGN FRAMEWORK

2.1 Overall System Architecture

Nuclear power electrical design is an engineering process that is **constrained by standards, driven by rules, centered on documents, and organized around workflows**. Design activities span the full lifecycle from requirement definition, equipment selection, and engineering calculations to standard compliance checking and document generation.
To address these characteristics, we propose a four-layer integrated architecture consisting of:
1. A **User Interaction Layer**,
2. An **Intelligent Orchestration Layer**,
3. A **Multi-Agent Execution Layer**, and
4. A **Knowledge Enhancement Layer**.

The overall system architecture is illustrated in Figure 1, which shows how user intent flows through orchestration, agents, and knowledge services to yield standardized design documents.

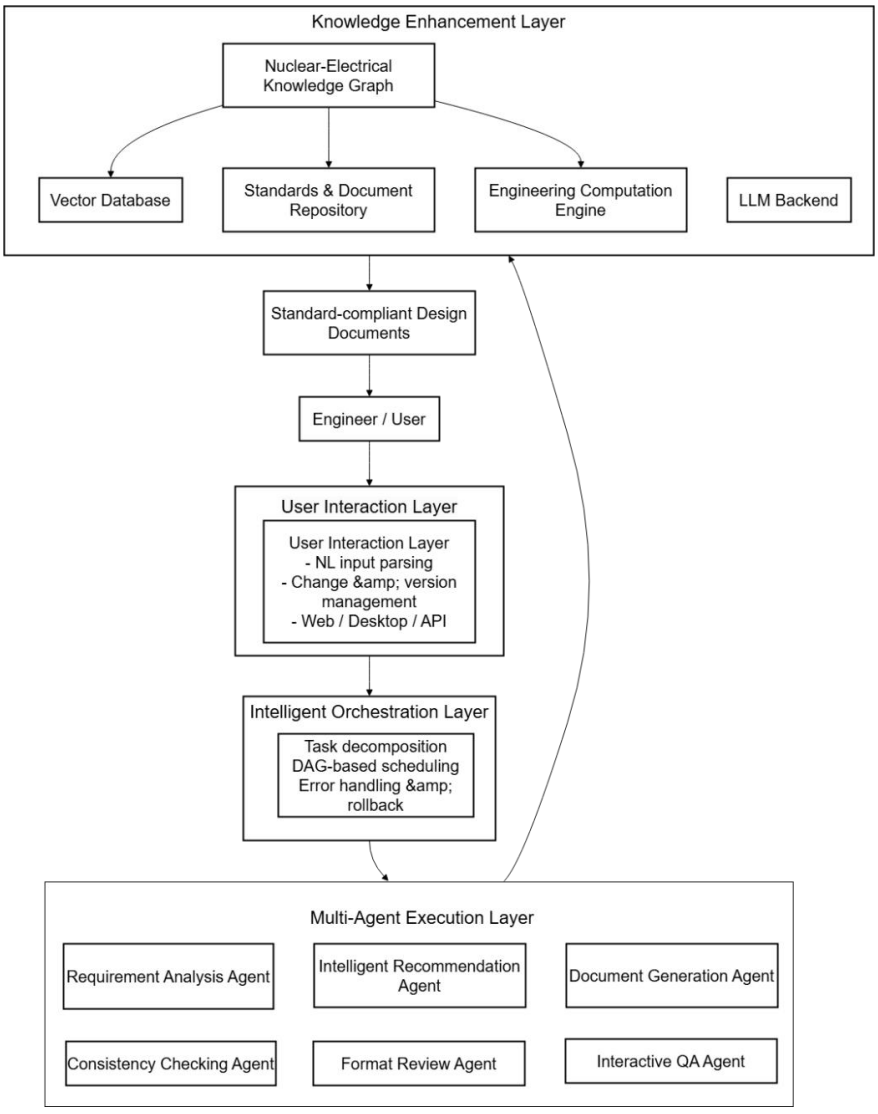

Figure 1 Overall Four-Layer Architecture of the Proposed Intelligent Nuclear Electrical Design System

2.1.1 User interaction layer

The user interaction layer serves as the interface between engineers and the system. It is responsible for:
- Transforming natural-language engineering intent into structured, machine-interpretable task descriptions;
- Supporting design change management, version control, and review comment handling;
- Providing web-based, desktop, and API interfaces for enterprise-wide collaborative design.

Its core objective is to ensure that user intent is accurately captured and represented, providing a clear context for subsequent intelligent design processes.

2.1.2 Intelligent orchestration layer

The intelligent orchestration layer acts as the system's central controller. By decomposing, scheduling, and coordinating tasks, it manages the overall multi-agent collaboration process.

Key mechanisms include:

- **Task decomposition:** Breaking down complex nuclear electrical design problems into manageable subtasks such as parameter acquisition, equipment selection, calculation checking, and document generation;
- **Dependency modeling:** Representing task dependencies using a directed acyclic graph (DAG);
- **Topological scheduling:** Executing tasks in an order that strictly respects logical and regulatory constraints;
- **Asynchronous messaging:** Enabling robust communication and data sharing among agents;
- **Exception handling and rollback:** Supporting error diagnosis, failure handling, and automatic retry when checks fail.

An illustrative example of the DAG-based task orchestration is shown in **Figure 2**, where nodes represent agents or computation modules and edges encode dependency and data flow relationships.

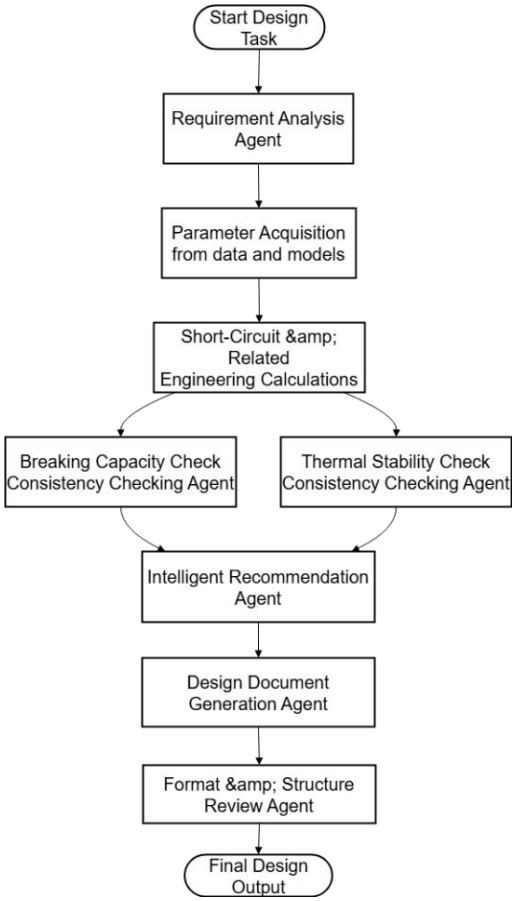

Figure 2 DAG-Based Task Orchestration for Nuclear Electrical Design

2.1.3 Multi-agent execution layer

The multi-agent execution layer consists of six specialized agents, each bound to specific knowledge subgraphs, business rules, and document templates, forming a role system with clear responsibilities and boundaries:

- **Requirement Analysis Agent:** Performs requirement structuring, constraint identification, and determination of relevant standards;
- **Intelligent Recommendation Agent:** Provides equipment selection and scheme recommendations based on standard constraints and calculation results;
- **Automatic Document Generation Agent:** Generates design documents, technical specifications, and calculation notes;
- **Consistency Checking Agent:** Validates the consistency and correctness of parameters, equipment selections, and standard clause references;
- **Format Review Agent:** Checks document structure and formatting against nuclear industry documentation norms;
- **Interactive QA Agent:** Provides explanations of design decisions, interpretations of standards, and real-time question answering.

This multi-agent architecture transforms nuclear electrical design from "manual division of labor" to "intelligent division of labor," resembling a digitalized in-house engineering team.

2.1.4 Knowledge enhancement layer

The knowledge enhancement layer provides the machine-understandable, retrievable, and inferable knowledge base needed by RAG, agents, and document generation. Its core components include:

- A nuclear electrical knowledge graph (standards, clauses, equipment parameters, design rules);
- A vector database for semantic retrieval;
- A document repository containing standards, drawings, and technical manuals;
- An engineering computation engine (short-circuit current, thermal stability, cable ampacity, etc.);
- Large language models for generation, reasoning, and dialogue.

Graph-RAG retrieval, agent reasoning, and document generation all rely on this layer. The end-to-end intelligent design workflow across these layers is depicted in **Figure 3**.

2.2 Formal Modeling of Nuclear Electrical Design Tasks

To make the design process formal, computable, and verifiable, we model the nuclear electrical design task as a mathematical object.

A design task is defined as a quintuple:

$$T = (R, C, K, O, D) \tag{1}$$

where:

- R(Requirements): a set of requirements, including functional requirements, performance metrics, and environmental conditions;
- C(Constraints): a set of constraints, including hard constraints (e.g., core safety clauses) and soft constraints (e.g., recommended clauses);
- K(Knowledge): a knowledge base containing standards, equipment data, formulas, and engineering cases;
- O(Objectives): design objectives such as maximizing safety margin, balancing cost and performance, and maximizing reliability;
- D(Design Outputs): outputs including selection results, calculation tables, and technical documents.

Example: short-circuit breaking capacity constraint

For a circuit breaker, the breaking capacity constraint can be expressed as:

$$c_1: I_{cu} \geq k \cdot I_k \tag{2}$$

where:

- I_{cu}: rated short-circuit breaking capacity;
- I_k: expected short-circuit current at the installation point;
- k: safety factor defined in IEC/GB standards.

Example: seismic qualification requirement for safety-class equipment

For safety-class equipment, a typical constraint is:

$$c_2: \text{SafetyClass}(e) = 1E \Rightarrow \text{SeismicQualified}(e) = \text{True} \tag{3}$$

This formalization provides the mathematical basis for agent reasoning, computation, and checking, and it underpins the verifiability and traceability of automation.

2.3 Intelligent Design Workflow

Starting from user design intent, the intelligent design workflow proceeds through requirement structuring, knowledge retrieval, engineering calculations, multi-agent collaboration, and standardized document generation, forming a complete and closed-loop design process. The overall workflow and its main stages are illustrated in **Figure 3**.

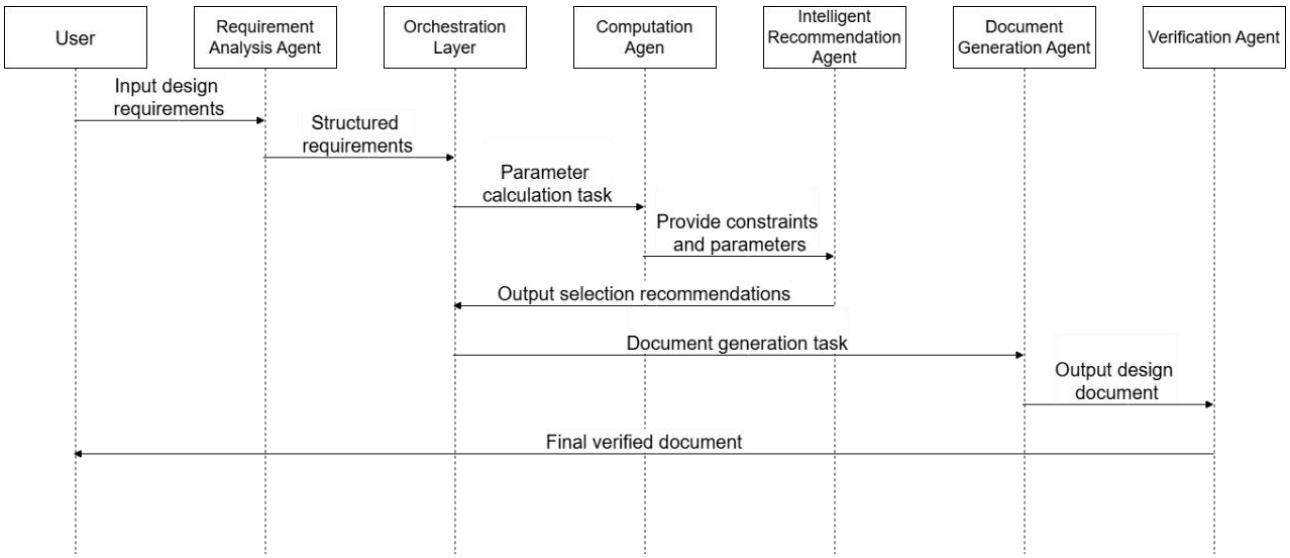

Figure 3 End-to-end Intelligent Workflow from Engineering Intent to Standardized Design Documents

From a technical perspective, the workflow exhibits the following core characteristics:

2.3.1 Automatic mapping from intent to structured tasks

The Requirement Analysis Agent semantically parses natural-language user input and, based on the domain ontology and constraint models in the knowledge graph, decomposes complex requirements into:

- Design objectives;
- Functional requirements;
- Performance metrics;
- Safety constraints.

This enables the system to interpret design instructions as "engineering task units," ensuring that downstream steps are well-defined and executable.

2.3.2 Graph-RAG as the core knowledge support mechanism

During design execution, the system does not rely solely on the internal parameters of an LLM. Instead, it uses a Graph-RAG retrieval module to:

- Extract authoritative constraint conditions from standard clauses;
- Identify equipment entities, parameter relations, and multi-hop reasoning chains from the knowledge graph;
- Retrieve relevant cases and historical design rationales from the document corpus.

The retrieved knowledge is organized into **evidence chains** and passed along with task context to the agents. This evidence-based paradigm effectively mitigates hallucinations and ensures that agents operate under a rigorous standard framework.

2.3.3 Collaborative multi-agent processing for parallelism and division of labor

After task decomposition, the Intelligent Orchestration Layer constructs a DAG over subtasks, enabling:

- **Serial tasks** that must follow a strict design order (e.g., short-circuit calculation → breaking capacity checking);
- **Parallel tasks** that are independent (e.g., short-circuit calculations at multiple buses);
- **Iterative tasks** that require re-generation (e.g., if a consistency check fails, control is passed back to a generation agent for revision).

Each agent has clearly defined boundaries, dedicated knowledge subgraphs and rule sets, and structured communication channels, resembling a well-organized digital design team.

2.3.4 Automation of engineering computation and standard checking

The computation-related agents automatically perform engineering calculations such as short-circuit currents, thermal stability checks, and cable ampacity assessments by calling:

- Formula libraries;
- Parameter models;
- Typical equipment values;
- Standard constraints encoded in the knowledge graph.

The results are then validated by the Consistency Checking Agent, ensuring that outputs can be traced back to specific standard clauses and explicit calculation steps.

2.3.5 Structured and standardized document generation

The Automatic Document Generation Agent uses:

- Template libraries of technical specifications;
- Document formatting standards;
- Evidence chains and intermediate calculation results,

to generate comprehensive design documents, including:
- Design descriptions;
- Technical specifications;
- Equipment lists;
- Calculation notes.

After processing by the Format Review Agent, documents are standardized in layout, chapter numbering, and clause referencing, satisfying formal nuclear industry delivery requirements.

2.3.6 Traceable, verifiable, and explainable design loop

Each step in the workflow produces:
- Execution logs;
- Retrieval records;
- Lists of referenced standard clauses;
- Data version identifiers.

This yields a highly transparent and auditable design process, providing strong support for safety reviews and regulatory inspections.

3 KEY TECHNICAL METHODS

3.1 Construction of a Nuclear Power Electrical Knowledge Graph

The nuclear power electrical knowledge graph (Nuclear-Electrical KG) serves as the core knowledge backbone of the system. It provides the structured data foundation for Graph-RAG retrieval, agent reasoning, and design checking. The construction process consists of four stages: ontology design, knowledge extraction, knowledge fusion, and quality assessment.

3.1.1 Ontology design

To make nuclear electrical domain knowledge machine-understandable, retrievable, and inferable, we adopt the Web Ontology Language (OWL) to build a three-layer ontology comprising an **upper ontology**, a **domain ontology**, and an **application ontology**. This layered structure balances conceptual abstraction with engineering semantics and provides a unified schema for knowledge fusion, relation reasoning, and Graph-RAG retrieval. The overall ontology schema is illustrated in **Figure 4**.

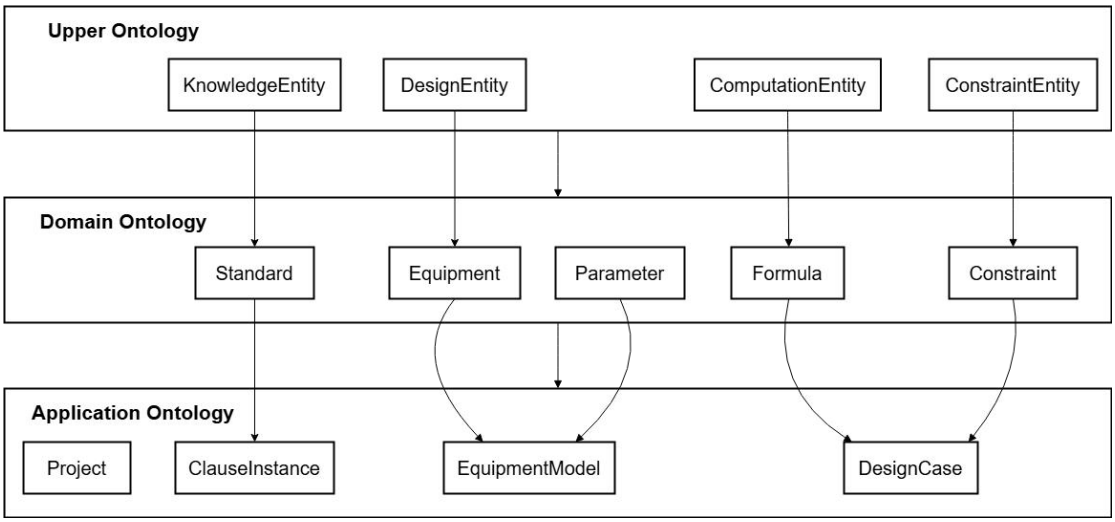

Figure 4 Three-Layer Ontology Schema for the Nuclear Electrical Knowledge Graph

(1) Upper ontology

The upper ontology captures the most general and abstract semantics of engineering design and serves as the foundational structure of the knowledge graph. It defines cross-domain shared classes and relations to ensure semantic consistency across heterogeneous sources.

Core classes include:
- **DesignEntity:** abstract representation of all design objects, such as equipment, systems, and components;
- **KnowledgeEntity:** representation of knowledge sources such as standards, clauses, and documents;
- **ConstraintEntity:** representation of engineering constraints, including safety classes, environmental conditions, and installation requirements;
- **ComputationEntity:** representation of computational procedures, formulas, input/output parameters, and related mathematical structures.

(2) Domain ontology

The domain ontology provides structured modeling of professional knowledge specific to nuclear electrical design. It defines entities, attributes, and constraints in engineering terms to ensure rigor and domain specificity.
Key modeling objects include:
a) **Standard classes:** covering frequently used mandatory and recommended standards, such as IEC international standards, GB national standards, DL power industry standards, NB nuclear standards, and HAF nuclear safety regulations. These are linked to equipment and constraints via relations such as *refersTo*, *constrains*, and *appliesTo*.
b) **Equipment classes:** including major electrical equipment such as circuit breakers, transformers, cables, and protection devices, each with attributes such as rated current, impedance, breaking capacity, insulation level, and environmental category.
c) **Parameter classes:** describing key variables in design calculations, e.g., rated current, impedance, breaking capacity, and capacity, which are associated with formulas and equipment via *hasValue*, *hasUnit*, and *usedInFormula*.
d) **Formula classes:** representing short-circuit current, cable ampacity, voltage drop, and other engineering formulas, with detailed definitions of input/output parameters, applicability conditions, and source standards.
e) **Constraint classes:** encoding typical nuclear engineering constraints such as safety class 1E requirements, seismic categories, environmental qualification categories (e.g., K1/K2/K3), temperature rise limits, fire protection requirements, and EMC constraints.
These entities and relations provide the logical basis for automatic checking and decision support.

(3) Application ontology

The application ontology instantiates the ontology using concrete engineering projects, plant types, and actual standard clauses, forming an "engineering knowledge network" suitable for project-level reasoning.
Its main objectives are to:
- Recognize specific equipment types and models used in real projects;
- Capture dependency relations among plant subsystems and components;
- Support cross-clause semantic reasoning;
- Provide traceable knowledge chains linking design data to specific standard clauses.

Key contents include:
- Instantiated standard clauses (e.g., specific articles from HAF102-2016);
- Equipment models with bound parameter values;
- Historical project design cases;
- Cross-references among clauses;
- Complete logical chains from equipment entities to parameters, formulas, and standards.

3.1.2 Knowledge extraction

Knowledge sources include standard texts, equipment manuals, engineering documents, and historical project records. We adopt a hybrid strategy combining deep learning, rule-based extraction, and manual validation.
- **Entity recognition (NER):** Domain-adapted BERT-based NER models are trained to identify entities such as equipment names, standard numbers, parameter names, and environmental categories.
- **Relation extraction:** Datasets are built using distant supervision supplemented by manual correction. Relations such as equipment-parameter, standard-clause, and clause-constraint are extracted, and multi-hop reasoning chains (e.g., standard → equipment type → parameters) are supported.
- **Attribute extraction:** Structured documents are parsed using rule-based methods, whereas unstructured texts are processed with sequence labeling models such as BiLSTM and Transformer architectures.

3.1.3 Knowledge fusion and conflict resolution

To resolve conflicts across heterogeneous sources such as different standards and equipment manuals, we employ:
- **Entity alignment:** based on vector embeddings and string similarity features;
- **Relation normalization:** mapping extracted relations onto ontology-defined schema;
- **Conflict resolution:** using an authority-weighted strategy (national standards > industry standards > corporate standards);
- **Recency preference:** prioritizing the latest versions of standards.

3.1.4 Knowledge graph quality assessment

The knowledge graph is evaluated along four dimensions:
- **Completeness:** coverage of key entities, relations, and attributes in the domain;
- **Accuracy:** correctness of extracted entities, relations, and attributes;
- **Consistency:** logical and semantic coherence under the ontology schema;
- **Freshness:** timeliness of standard versions and equipment data.

This evaluation ensures that the knowledge graph is reliable and suitable for safety-critical design tasks.

3.2 Graph-Guided Hybrid Retrieval-Augmented Generation (Graph-RAG)

Graph-RAG is a core innovation of this study. By integrating a structured knowledge graph with vector-based retrieval, it provides high-precision knowledge recall and enables evidence-based generation. Recent surveys have shown that such graph-enhanced RAG approaches can significantly improve retrieval quality and interpretability [9-12].

3.2.1 Three-path hybrid retrieval

We adopt a three-path hybrid retrieval strategy:

- Path 1: Semantic vector retrieval

Queries and documents are encoded into dense vectors. This is suitable for fuzzy semantic matching and long texts, and it provides high recall.

- Path 2: Knowledge graph retrieval

Natural-language queries are transformed into SPARQL or graph queries. This path supports multi-hop relational reasoning and can extract logically coherent knowledge chains from the graph.

- Path 3: BM25 keyword retrieval

BM25 is used for precise matching of standard numbers, technical terms, and formulas, and offers robustness and speed for structured engineering documents.

3.2.2 Retrieval result fusion

We use a multi-factor scoring function:

$$\text{Score}_{\text{final}} = w_1 S_{\text{rel}} + w_2 S_{\text{auth}} + w_3 S_{\text{fresh}} + w_4 S_{\text{cite}} \quad (4)$$

where:

- S_{rel}: semantic relevance score;
- S_{auth}: authority score (prioritizing higher-level standards and regulations);
- S_{fresh}: freshness score (favoring newer versions);
- S_{cite}: citation frequency (frequency of usage in historical designs).

A cross-encoder-based re-ranking model is then applied to the candidate results, and the top 5-10 passages are selected as high-confidence evidence for downstream agents.

3.2.3 Context engineering and evidence chain construction

To avoid hallucinations, all retrieved evidence is passed to the LLM in the form of **evidence chains**, which include:

- Graph reasoning paths;
- Original standard clause texts;
- Parameter provenance information;
- Conflict annotations and resolution results.

This approach ensures that each generated fragment can be traced back to specific standard clauses and equipment data. It aligns with recent work on knowledge-graph-enhanced RAG and graph-enhanced agent architectures.

3.3 Multi-Agent Collaboration based on Large Language Models

3.3.1 Agent role definition and boundary control

To ensure that agents are controllable, explainable, and auditable, each agent is bound to:

- A specific knowledge subgraph;
- A subset of standard clauses;
- Dedicated document templates;
- A business rule set;
- A defined communication protocol.

This design ensures that each agent's outputs can be checked and validated against its responsibilities, and that errors can be localized.

3.3.2 DAG-based orchestration and scheduling

The system uses a DAG as the backbone of task orchestration:

- **Serial tasks:** tasks that must follow a strict order, such as "short-circuit calculation → breaking capacity check";
- **Parallel tasks:** independent tasks that can be executed concurrently, such as short-circuit calculations at multiple buses;
- **Iterative tasks:** tasks that must be repeated if checks fail, such as "consistency check fails → regenerate design parameters."

An example of DAG-based agent orchestration is shown in **Figure 2**, and a more detailed view of the execution process is illustrated in **Figure 6** during the validation discussion.

3.3.3 Inter-agent communication

We define four main types of inter-agent messages:

- Task assignment messages;
- Intermediate data exchange messages;
- Status update messages;
- Conflict negotiation messages.

These communication patterns underpin stable and interpretable collaboration among agents and ensure the consistency of shared context.

4 METHOD VALIDATION AND ANALYSIS

To verify the feasibility and effectiveness of the proposed Graph-RAG + MAS method in nuclear electrical design, we perform a descriptive validation based on typical engineering tasks, system behavior, key technical performance, and practical engineering value. Although a full-scale quantitative evaluation is beyond the scope of this work, simulated task execution, clause-level comparison, and expert interviews provide a systematic basis for assessing the method's applicability and deployment potential.

4.1 Overall Validation Approach

In nuclear electrical engineering, system validation cannot rely solely on simple numerical indicators; instead, it emphasizes:

- The completeness of the design workflow;
- The accuracy and appropriateness of knowledge usage;
- The rationality of logical chains;
- The structural and stylistic quality of document outputs.

Our validation approach includes:

- Selecting representative nuclear electrical design tasks;
- Preparing a corpus of standards, equipment data, and engineering documents;
- Simulating multi-round design execution under the proposed system;
- Inviting senior engineers to evaluate the design results.

The overall validation procedure—from task definition and corpus construction to system execution and expert evaluation—is summarized in **Figure 5**.

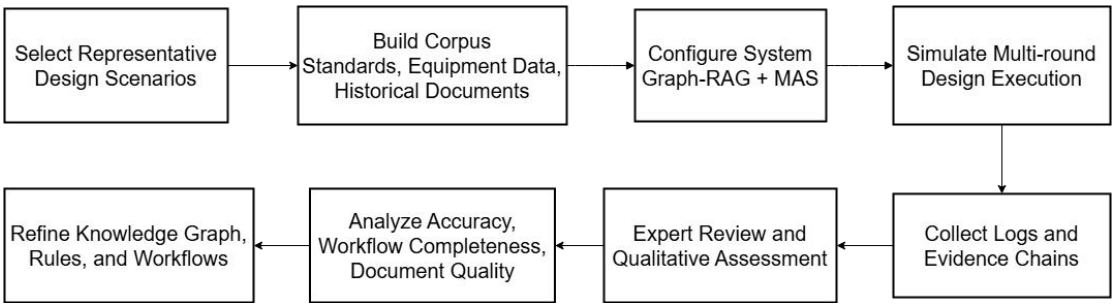

Figure 5 Validation procedure for the proposed Graph-RAG + MAS method

4.2 Validation Scenarios

To cover both **calculation-oriented tasks** and **document-oriented tasks**, we select two typical scenarios.

4.2.1 Scenario 1: Low-voltage circuit breaker selection

This scenario captures the characteristic features of nuclear design tasks involving chained logical reasoning, standard referencing, and engineering computation. The task involves:

- Parsing load parameters;
- Selecting and applying short-circuit calculation methods;
- Checking breaking capacity and thermal stability;
- Identifying safety class (e.g., 1E and environmental categories);
- Recommending equipment models under relevant constraints;
- Automatically generating a draft technical specification.

This scenario tests:

- The accuracy of Graph-RAG in retrieving relevant standard clauses;
- The traceability and correctness of the computation process;
- The quality of inter-agent collaboration;
- The completeness and compliance of the generated document.

An example of the DAG execution process for this scenario, including agent interactions and data flows, is illustrated in **Figure 6**.

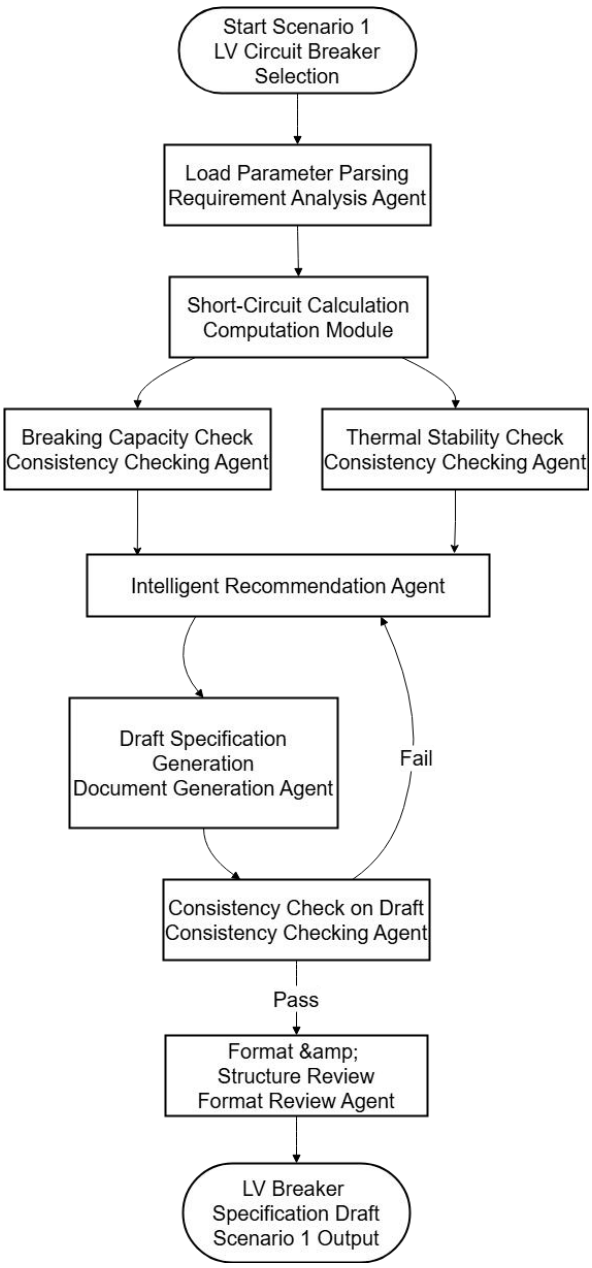

Figure 6 Example DAG Execution for Scenario 1: Low-Voltage Circuit Breaker Selection

4.2.2 Scenario 2: Technical specification for 1E-class switchgear

This scenario focuses on the system's capabilities for long-document generation, clause composition, and document structuring. The task involves:

- Determining applicable standards based on safety class;
- Automatically identifying constraints on switchgear compartmentalization, environmental qualification, and EMC;
- Retrieving 1E equipment-related content from the knowledge graph;
- Organizing the document structure into sections and subsections;
- Generating main chapters such as environmental conditions, performance requirements, and testing requirements;
- Producing a standardized technical specification draft.

This scenario tests:

- The system's global understanding of the standard system;
- Its ability to combine knowledge from multiple sources;
- The correctness of document hierarchy and structure;
- Its mastery of engineering writing style.

Expert feedback indicates that the generated documents exhibit clear logic, complete chapter structures, and accurate clause references, making them suitable as initial drafts for engineering use.

4.3 Analysis of Graph-RAG Retrieval Enhancement

Accurate retrieval of standard clauses and equipment parameters is central to design tasks. Observations suggest that Graph-RAG offers clear advantages over pure vector-based RAG:

4.3.1 Engineering-aware retrieval

By exploiting entity relations and clause dependencies in the knowledge graph, Graph-RAG can:

- Filter out irrelevant content based on standard-chapter-clause hierarchy;
- Automatically focus on test requirements and applicability ranges specific to the equipment type;
- Expand retrieval scope along graph paths to avoid missing key clauses.

4.3.2 Logically coherent results

Graph-RAG provides "clause chains" that explicitly show how clauses reference and constrain each other. This is critical in nuclear engineering because:

- Clauses often cannot be interpreted in isolation;
- Calculation conditions are frequently defined jointly by multiple chapters;
- Equipment selection must satisfy multiple interacting constraints.

4.3.3 Higher authority of retrieved content

The system prioritizes higher-level sources when fusing retrieval results:

- National standards (GB);
- Industry and nuclear standards (DL, NB, HAF);
- IEC international standards.

Consequently, the generated content aligns well with engineers' implicit hierarchy of standard authority.

4.4 Analysis of Multi-Agent Collaborative Design

In multiple simulated runs, the MAS demonstrates good stability and interpretability.

4.4.1 Clear division of labor and boundaries

Each agent is associated with different knowledge subgraphs, standard packages, and rule sets, which leads to:

- Outputs that reflect distinct role responsibilities;
- Clear error localization when issues arise;
- Non-overlapping decision boundaries.

For example, the Requirement Analysis Agent does not perform numerical calculations, the computation-related agents do not generate long-form documents, and the Document Generation Agent does not define technical calculation logic. Engineers note that this division of labor closely mirrors real design team collaboration patterns.

4.4.2 Smooth orchestration and clear logical chains

DAG-based orchestration ensures that task dependencies strictly follow nuclear design workflows. The orchestrator dynamically schedules serial, parallel, and iterative tasks according to dependency constraints and agent outputs. An illustrative example of this process is shown in Figure 6, which highlights the coordination among agents and the propagation of evidence chains.

4.4.3 Positive human-AI interaction

During design execution, the Interactive QA Agent provides:

- Explanations of standard clauses;
- Clarifications of parameter definitions;
- Justifications of design decisions.

This functionality significantly increases the transparency of AI behavior and reduces the "black-box" perception common in LLM-based systems.

4.5 Quality and Engineering Usability of Generated Documents

In multiple tasks, the Document Generation and Format Review Agents exhibit the following strengths:

4.5.1 Document structure aligned with nuclear industry practice

The generated chapter organization closely matches the structure of standard nuclear engineering templates, including:

- Scope;
- Normative references;
- Operating environment;
- Technical requirements;
- Test requirements;
- Appendices and data sheets.

The structure is complete, logically ordered, and convenient for review.

4.5.2 Appropriate engineering writing style

The generated text typically exhibits:

- A rigorous and objective tone;
- Reasonable paragraphing and sectioning;
- Clear indication of clause sources;
- Appropriate use of domain-specific terminology.

This yields documents with high engineering usability.

4.5.3 Traceable design rationale

Documents explicitly or implicitly annotate:

- Source standards;
- Knowledge graph entities;
- Constraints;
- Reasoning chains.

This greatly facilitates document review, re-checking, and regulatory auditing.

4.6 Engineering Feedback and Application Prospects

Expert interviews and repeated system runs suggest that:

- The method significantly reduces manual standard lookup and repetitive calculation work;
- Generated documents are close to actual design documents and suitable as drafts or auxiliary materials;
- The system's understanding and referencing of standards are highly reliable, supporting normalized design;
- The MAS architecture can be extended to additional subdomains such as protection, automation, and grounding;
- The overall methodology is practically deployable as an internal intelligent design platform for nuclear power enterprises.

These observations are consistent with prior experience in building knowledge-graph-based decision-support systems for nuclear safety review.

5 CONCLUSION

This paper proposes an intelligent nuclear power electrical design methodology that integrates knowledge-graph-enhanced retrieval-augmented generation (Graph-RAG) with a multi-agent system (MAS). The method addresses key challenges in nuclear electrical design, including an extensive standard, difficult knowledge reuse, and the limited reliability of general-purpose LLMs in specialized domains.

We construct a domain knowledge graph covering standards, equipment parameters, and design rules, providing a structured knowledge backbone. A graph-guided hybrid retrieval strategy is designed to integrate vector retrieval, knowledge graph retrieval, and BM25 retrieval. A multi-factor scoring and re-ranking mechanism significantly improves retrieval accuracy and effectively reduces hallucinations. A multi-agent collaborative architecture—including requirement analysis, intelligent recommendation, automatic generation, consistency checking, format review, and interactive QA agents—is implemented, and DAG-based task orchestration enables parallel and dynamic execution of complex design workflows.

Theoretical analysis and representative engineering scenarios demonstrate that, compared with traditional methods, the proposed approach offers notable advantages in knowledge reliability, design traceability, collaboration efficiency, and quality assurance. Each design decision can be traced back to explicit standard clauses and equipment parameters, and intelligent checking mechanisms ensure the standard compliance of design documents. The method provides a feasible pathway for the intelligent transformation of nuclear power electrical design and a transferable technical reference for the intelligent upgrading of other complex engineering systems.

COMPETING INTERESTS

The authors have no relevant financial or non-financial interests to disclose.

FUNDING

This work is supported by the Talent Fund Project No. 25816 of China Institute of Atomic Energy (CIAE).

REFERENCES

[1] Ji Z, Lee N, Frieske R, et al. Survey of hallucination in natural language generation. ACM Computing Surveys, 2023, 55(12): 1-38.
[2] Lewis P, Perez E, Piktus A, et al. Retrieval-augmented generation for knowledge-intensive NLP tasks. In: Proceedings of NeurIPS, 2020: 9459-9474.
[3] Gao Y, Xiong Y, Gao X, et al. Retrieval-augmented generation for large language models: A survey. arXiv preprint arXiv:2312.10997, 2023.
[4] Peng B, Galkin M, He P, et al. Graph retrieval-augmented generation: A survey. arXiv preprint arXiv:2408.08921, 2024.
[5] Wang Y, Zhong Q, Liu L, et al. A survey on LLM-based multi-agent systems: Workflow, infrastructure, and challenges. Autonomous Agents and Multi-Agent Systems, 2024, 38(2): 1-35.
[6] Buehler M J. Generative retrieval-augmented ontologic graph and multi agent strategies for interpretive large language model-based materials design. arXiv preprint arXiv:2310.19998, 2023.

[7] Huang Q, Peng S, Deng J, et al. A review of the application of artificial intelligence to nuclear reactors: Where we are and what's next. Heliyon, 2023, 9(10): e13883.
[8] Guo, C, Yi, Y, Luo, W, et al. Design and prototype implementation of a nuclear power plant safety review decision-support system based on knowledge graphs. Nuclear Safety, 2024, 23(3): 55-62
[9] Yang R, Xue H, Razzak I, et al. Divide by question, conquer by agent: SPLIT RAG with question driven graph partitioning. arXiv preprint arXiv:2505.13994, 2025.
[10] Wang S, Fan W, Feng Y, et al. Knowledge graph retrieval-augmented generation for LLM based recommendation. arXiv preprint arXiv:2501.02226, 2025.
[11] Zhu X, Xie Y, Liu Y, et al. Knowledge graph-guided retrieval augmented generation. In Proceedings of the 2025 Conference of the Nations of the Americas Chapter of the Association for Computational Linguistics: Human Language Technologies. Albuquerque, New Mexico. Association for Computational Linguistics, 2025: 8912-8924. DOI: 10.18653/v1/2025.naacl-long.449.
[12] Shen H, Diao C, Vougiouklis P,et al. GeAR: Graph-enhanced agent for retrieval-augmented generation. arXiv preprint arXiv:2412.18431, 2024.

Journal of Computer Science and Electrical Engineering
Print ISSN: 2663-1938
Online ISSN: 2663-1946
DOI: https://doi.org/10.61784/jcsee3107

RECOGNITION OF CITRUS PLANTING AREA BY INTEGRATING PYRAMID BOTTLENECK RESIDUAL NETWORK AND DECISION TREE ALGORITHM

Yue Deng, KaiMing Zeng*
Jiangxi Institute of Territorial Space Surveying and Planning, Nanchang 330029, Jiangxi, China.
**Corresponding Author: KaiMing Zeng*

Abstract: As the agricultural cornerstone of Ganzhou, Jiangxi Province, China, citrus production necessitates rapid and precise mapping of orchard spatial distribution for agricultural management, resource assessment, ecological conservation, and science-driven industry development. Remote sensing has emerged as a vital agricultural informatics tool in China due to its non-contact, large-scale data acquisition capabilities. Recent advances in deep neural networks enable state-of-the-art solutions for image processing and computer vision tasks. Capitalizing on this, we propose a multispectral remote sensing framework integrating a Pyramid-Shaped Residual Network with a decision tree algorithm customized for citrus cultivation patterns. The results indicate that the new method demonstrates extremely high accuracy, with an estimation precision exceeding 80% when compared to the statistical yearbook. This approach demonstrates significant potential for citrus planting area identification, providing a valuable reference for precision agriculture applications.
Keywords: Citrus plantation area identification; Multi-spectral; Deep neural network; Pyramid residual

1 INTRODUCTION

Citrus, as the world's largest fruit crop, leads in both planting area and production. China, as one of its primary origins, boasts abundant resources and diverse varieties. The Gannan region, known as the "World Orange Town," has vigorously developed citrus cultivation since the 1980s. Today, its planting area and annual output consistently rank among the top in the country, making it a dominant force in the Gannan fruit market and a significant contributor to the economic development of southern China[1]. It serves as a backbone industry for rural revitalization and farmer income growth. In recent years, the government has actively promoted the upgrading of the citrus industry through policies and economic measures. However, the expansion of planting areas driven by growing market demand has also triggered ecological and production challenges. Citrus is cultivated in red soil, a typical ecologically fragile zone. Many new orchards have been converted from forests and farmland, where tree felling and farmland encroachment threaten biodiversity and impact grain yields[2]. Additionally, frequent natural disasters such as pests, diseases, and frost damage have led to tree deaths and fluctuations in planting areas, resulting in unstable production and prices, which in turn affect the economic livelihoods of residents. Against this backdrop, scientific monitoring of citrus cultivation has become particularly urgent.

Remote sensing technology, with its advantages of wide coverage, rapid information acquisition, and low cost, has been widely applied in agriculture[3]. It plays a crucial role in extracting area information, monitoring growth conditions, estimating yields, and detecting and preventing crop pests and diseases[4]. In citrus planting information extraction, compared to traditional field surveys, remote sensing enables large-scale dynamic monitoring, quickly and accurately obtaining orchard spatial distributions, significantly improving the efficiency and scientific rigor of information extraction. However, Ganzhou City is located in the hilly and mountainous regions of southern China, characterized by significant topographic undulations and diverse landforms, including mountains, hills, gorges, and rivers[5]. The fragmentation of land parcels results in weaker spatial connections between land objects, uneven distributions, and diverse vegetation communities, which complicates crop classification. Traditional machine learning extraction methods, such as Random Forest and Support Vector Machine models, are severely affected by the same object, different spectra effect and interference from multi-source background information. The extraction results often exhibit salt-and-pepper noise, with low accuracy. Object-oriented methods require frequent human-computer interaction, making it difficult to determine the segmentation scale for fragmented and irregular citrus planting areas. These methods inadequately mine complex features in the imagery, leading to limited extraction accuracy that struggles to meet practical application requirements. Additionally, cloudy and rainy weather in southern China affects the revisit cycles of medium- and high-resolution satellite data[6].

Deep neural networks are characterized by high automation and wide applicability, enabling automatic and in-depth extraction of image feature information with minimal interference from background information. In recent years, deep learning-based deep neural networks have emerged as advanced machine learning techniques, capable of addressing various tasks in image processing, computer vision, signal processing, and natural language processing. Deep learning has made significant progress in image classification tasks. In 2012, Krizhevsky et al.[7] proposed the convolutional neural network (CNN) architecture AlexNet[8], which won the ImageNet Large-Scale Visual Recognition Challenge.

Subsequently, VGG and GoogleNet surpassed AlexNet's record on ImageNet. However, when attempting to use deeper networks to improve classification accuracy, issues such as gradient explosion, gradient vanishing, and network convergence arise, making it difficult to increase network complexity and leading to degraded classification performance. To address these problems, the residual network (ResNet) introduced the concepts of residual learning and identity shortcut connections, effectively mitigating the aforementioned issues[9]. These methods have made it possible to train deeper network architectures. Paoletti et al.[10] proposed the Pyramid-Shaped Residual Network (PSSRN) by improving the SSRN. This method groups convolutional layers into pyramid residual modules and gradually increases the feature map dimensions across all convolutional layers, allowing the diversity of high-level spectral-spatial features to increase layer by layer, thereby achieving precise image classification.

This study selected Xingguo County, Ganzhou City, Jiangxi Province, China, as the research area. Utilizing multispectral remote sensing imagery and addressing challenges such as fragmented citrus planting plots, uneven distribution of land objects, and diverse vegetation communities, we conducted information extraction for citrus planting. We proposed a method combining a deep pyramid residual network with a decision tree tailored to citrus planting characteristics, achieving the identification of citrus planting areas in southern Jiangxi. The aim is to accurately grasp the spatial distribution of citrus planting, providing support for ecological protection, scientific yield estimation, and government decision-making.

2 MATERIALS AND METHODS

2.1 Study Area

Xingguo County (26°03′–26°44′N, 115°01′–115°52′E) is located in the south-central part of Jiangxi Province and the northern part of Ganzhou City, covering an area of 3,215 km². The topography is dominated by low mountains and hills, with red soil as the primary soil type. It belongs to a subtropical monsoon climate, with an average annual temperature of 18.9°C and an average annual precipitation of 1,522.3 mm (Figure 1).

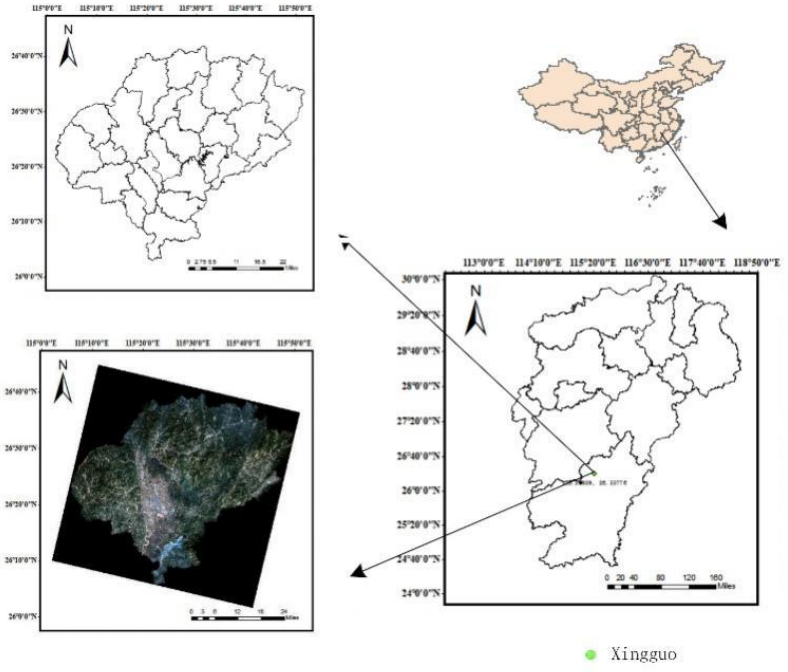

Figure 1 Location of the Study Area
Source: It was obtained from the Standard Map Service of the Ministry of Natural Resources of China. (available at: http://bzdt.ch.mnr.gov.cn/)

2.2 Data Source and Preprocessing

The remote sensing data of GF-1 were obtained from the China Centre for Resources Satellite Data and Application. GF-1 can acquire three types of remote sensing images: 2 m panchromatic (PAN), 8 m multispectral (MS), and 16 m multispectral (WFV) images. The revisit cycles for PAN and MS images are 41 days, while that for WFV images is 4 days. This study utilized WFV images acquired on December 6, 2020, November 27, 2021, December 21, 2022, and November 27, 2023. These data underwent preprocessing, including registration and clipping (Table 1).

Table 1 Parameters of GF-1 Satellite Data

GF-1 Data Type	PAN	MS	WFV
Spatial Resolution	2m	8m	16m

revisit period	41day	41day	4day
Spectral Range	450nm-900nm	Blue: 450nm-520nm Green: 520nm-590nm Red: 630nm-690nm Near-infrared: 770nm-890nm	

The digital elevation data (DEM) was sourced from NASA's Earthdata platform, with a spatial resolution of 12.5 m × 12.5 m. This resolution was resampled to match that of the WFV imagery, and the data was then integrated into the input of the deep neural network through band synthesis to utilize slope information in citrus planting area extraction.
The citrus planting area data of Xingguo County, Ganzhou City, Jiangxi Province, were sourced from the Jiangxi Statistical Yearbook (2020–2023). This data was used for classifier accuracy validation and annual assessment of citrus planting area extraction.

2.3 Method

2.3.1 Pyramid-Shaped Residual Network (PSSRN)

Paoletti et al. first introduced the Pyramid-Shaped Residual Network (PSSRN) for spectral-spatial classification of hyperspectral imagery. In the PSSRN structure, the number of feature maps output by each residual unit is not fixed but gradually increases, resembling a pyramid that widens from top to bottom[11]. The network consists of five modules: an input convolutional module (C), three pyramid modules (M1, M2, and M3), a pooling module (P), and a fully connected module (FC). Each pyramid module comprises three pyramid bottleneck residual units. The pooling module uses average pooling to downsample the output feature maps of the last pyramid module (M3) for the final time, reshaping them into vectors to be fed into the fully connected layer at the end of the network for classification. The input to the PSSRN is a multi-band multispectral image patch, and the output is the classification category. Excluding the input layer, output layer, BN layer, and ReLU layer, the entire network has a depth of 30 layers.
The PSSRN was designed for hyperspectral images, and the differences in spectral and spatial resolutions make it suboptimal for direct application to multispectral classification. To address this, we modified the model to adapt it to multispectral classification, considering the differences between the two types of images.
On one hand, multispectral images have superior spatial resolution compared to hyperspectral images. Due to the lower spatial resolution of hyperspectral data, smaller input image patches are sufficient to extract texture features effectively, achieving precise classification. In contrast, the high spatial resolution of multispectral images requires larger input image patches to fully extract texture features and enhance the distinction between different land cover types, thereby capturing neighborhood and non-local similarities within the images. Therefore, we increased the input image patch size to 27×27 to extract image features over a larger area. Additionally, considering the richness of details in multispectral images, we also reduced the filter size to extract details around each pixel, further improving classification accuracy.
On the other hand, multispectral images have far fewer bands than hyperspectral images. To match the scale of the input data and prevent overfitting, we reduced the number of convolutional kernels, decreasing the initial layer's convolutional kernel count from 103 to 64. The detailed architecture and parameters of the final network are illustrated in Table 2, where "conv" represents the convolutional layer, "BN" represents the batch normalization layer, and "ReLU" represents the activation layer.
To achieve classification, auxiliary preprocessing steps are required. First, the original multispectral image is normalized to zero mean and unit variance. Second, to utilize spectral-spatial information, a 3D neighboring block around each pixel is extracted, denoted as $M_{ij} \in R^{N \times d \times d}$, where N is the number of bands and d is the block size. The cubic block is then input into the model as the input data, with the boundary areas padded using the mirror method. The fully connected layer of the network uses softmax to output class labels.

Table 2 Proposed Deep Network Architecture

Modules	Units	Layers	Kernel size	Kernel numbers	Stride
C		conv	3×3	64	1
Pyramid Module M_1	Pyramid Bottleneck Residual Block $B(1)_1$	BN			
		conv	1×1	64	1
		BN, conv	5×5	32	1
		BN, conv	1×1	84	1
		Relu			
	Pyramid Bottleneck Residual Block $B(1)_2$	BN			
		conv	1×1	84	1
		BN,conv	5×5	42	1
		BN,conv	1×1	104	1
		Relu			
	Pyramid Bottleneck Residual Block $B(1)_3$	BN			
		conv	1×1	104	1
		BN, conv	5×5	52	1
		BN, conv	1×1	124	1
		Relu			

	Pyramid Bottleneck Residual Block $B(2)_1$	BN			
		conv	1×1	124	1
		BN,conv	6×6	62	2
		BN,conv	1×1	144	1
		Relu			
Pyramid Module M_2	Pyramid Bottleneck Residual Block $B(2)_2$	BN			
		conv	1×1	144	1
		BN,conv	5×5	72	1
		BN,conv	1×1	164	1
		Relu			
	Pyramid Bottleneck Residual Block $B(2)_3$	BN			
		conv	1×1	164	1
		BN, conv	5×5	82	1
		BN, conv	1×1	184	1
		Relu			
	Pyramid Bottleneck Residual Block $B(3)_1$	BN			
		conv	1×1	184	1
		BN,conv	6×6	92	2
		BN,conv	1×1	204	1
		Relu			
Pyramid Module M_3	Pyramid Bottleneck Residual Block $B(3)_2$	BN			
		conv	1×1	204	1
		BN,conv	5×5	102	1
		BN,conv	1×1	224	1
		Relu			
	Pyramid Bottleneck Residual Block $B(3)_3$	BN			
		conv	1×1	224	1
		BN,conv	5×5	112	1
		BN,conv	1×1	244	1
		Relu			
Pyramid Pooling Module P		Average Pooling			
Fully Connected FC	——	Fully Connected, soft max			

2.3.2 Combination algorithm of PSSRN and decision tree

Based on field surveys and literature reviews, we found that citrus cultivation is constrained by slope and elevation, which are influenced by topography. Therefore, DEM data can be incorporated into the PSSRN input. Citrus orchards exhibit a certain degree of sparsity, allowing vegetation coverage to serve as a decision-making reference. Additionally, factors such as slope and illumination shadows affect citrus planting. For example, the DN values of GF-1 imagery in the blue and near-infrared bands can be utilized as references. Consequently, we integrated the citrus extraction results from the optimized pyramid bottleneck residual network with a decision tree for comprehensive evaluation, ultimately forming a complete citrus planting area map for the study region (Figure 2).

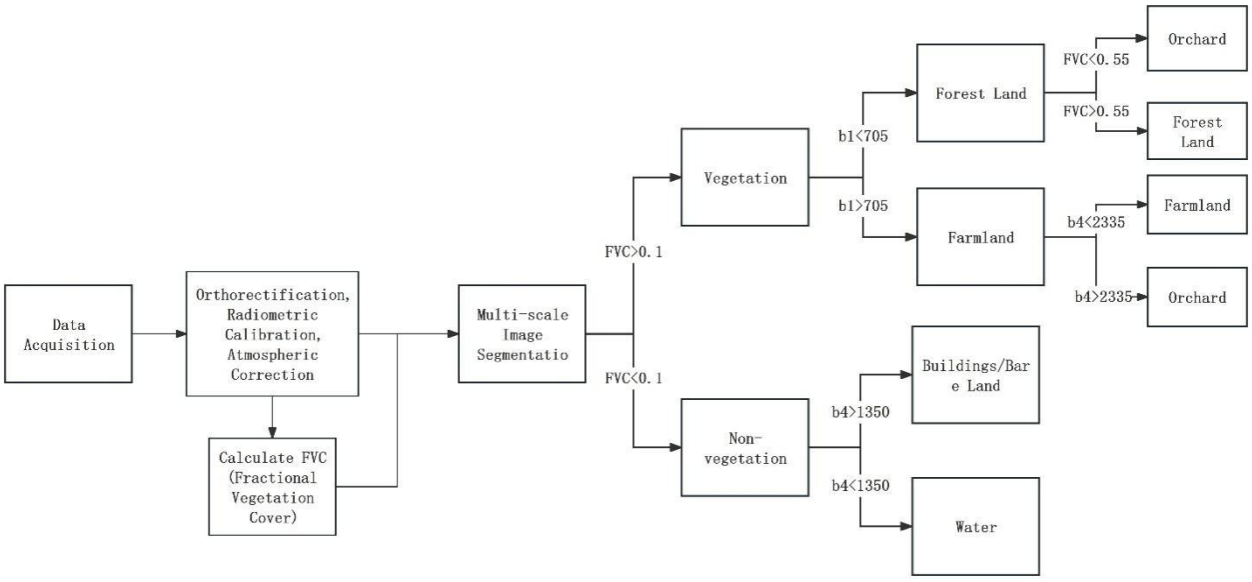

Figure 2 Citrus Planting Extraction Algorithm Combining PSSRN and Decision Tree

3 EXPERIMENTAL RESULTS

3.1 Recognition Result

The experimental setup includes an Intel(R) Xeon(R) E5-2620 v2 processor with 6M cache and 2.10 GHz (6-core/12-thread multitasking), 32GB RAM, an NVIDIA Tesla K20Xm GPU with 6GB VRAM, an 8TB Toshiba hard drive, and a Supermicro X9DRG-QF motherboard. The system runs on Red Hat Enterprise Linux Server release 6.4 x64, CUDA 9, cuDNN 7.2, Python 3.5, and a Keras framework.

In the first step, a pyramid bottleneck residual optimization network was used for citrus extraction. Randomly selected 10% of the labeled data was used as the training set, while the remaining labeled pixels served as the test set. After hyperparameter tuning, the network optimization algorithm employed stochastic gradient descent (SGD) with 200 training epochs. A variable learning rate was used during training, and the input multi-band image patch size was set to 27×27. In this study, we conducted a first-level classification, categorizing land cover types into forest, farmland, water, artificial building (including roads, etc.), bare land classes. To extract citrus planting areas, we added the "orchard" class, resulting in a total of six categories. The final classification results are as follows (Figure 3).

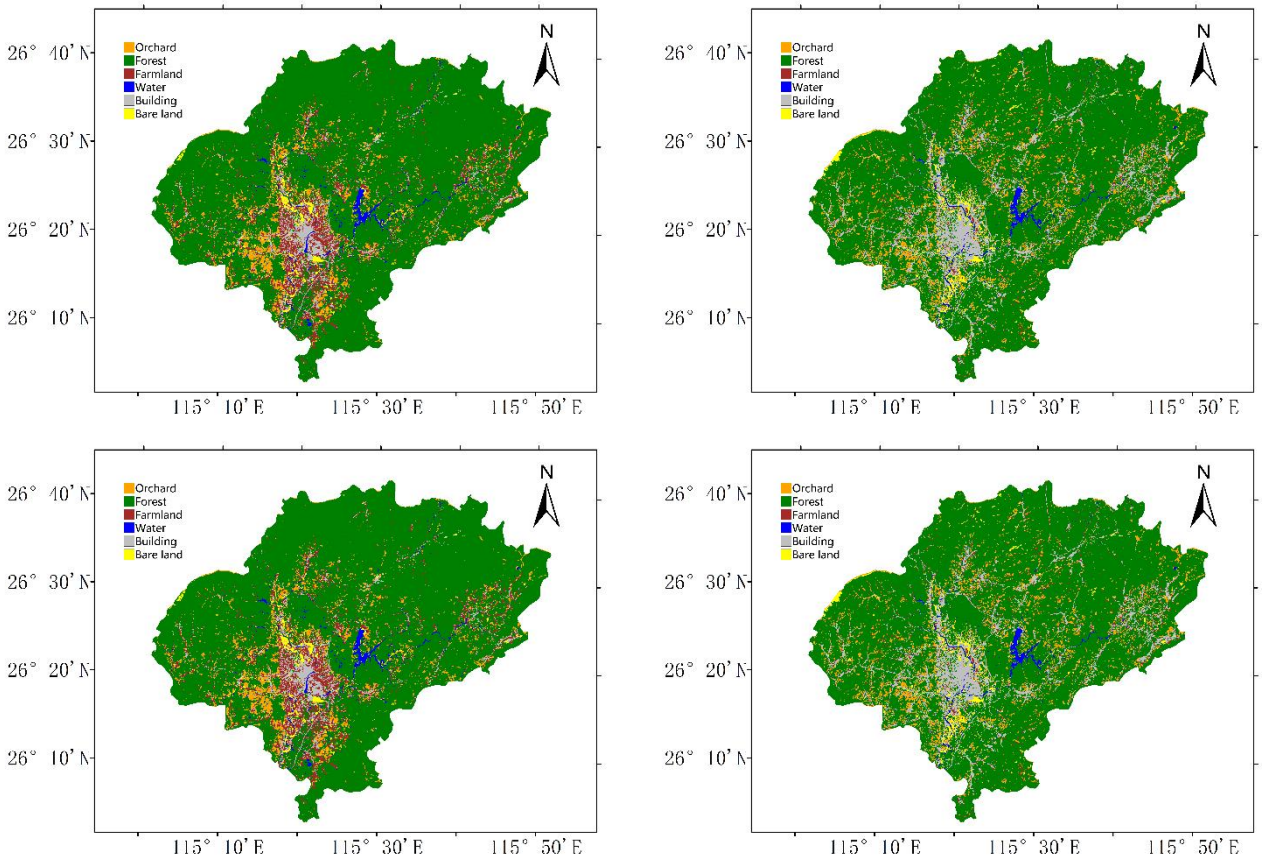

Figure 3 Results of Citrus Planting Areas in Xingguo County (2020–2022) Using GF-1 Satellite Data
Source: It was obtained from the Standard Map Service of the Ministry of Natural Resources of China. (available at: http://bzdt.ch.mnr.gov.cn/)

3.2 Accuracy Calculation

In this study, we adopted accuracy, precision, overall classification accuracy, and the Kappa coefficient as metrics to evaluate classification performance (Table 3).

Table 3 Accuracy and Precision Metrics

TP	The true class is positive, and the model predicts it as positive.
FP	The model predicts positive, but the true class is negative (inconsistent prediction).
FN	The model predicts negative, but the true class is positive (inconsistent prediction).
TN	The true class is negative, and the model predicts it as negative.

Accuracy represents the proportion of correctly predicted samples (TP and TN) among all samples. When the dataset is imbalanced, accuracy may not effectively reflect model performance. High accuracy can coexist with all minority class samples being misclassified; in such cases, other model evaluation metrics should be considered.The accuracy is calculated as follows:

$$\text{Accuracy} = (TP + TN) / \text{all data} \quad (1)$$

Precision for the positive class indicates the proportion of true positive samples among all samples predicted as positive. The precision is calculated as follows:

$$\text{Precision} = TP / (TP + FP) \quad (2)$$

Overall accuracy represents the proportion of correctly classified pixels among the total pixels, where the ground truth image or region of interest defines the true classification. Correctly classified pixels are distributed along the diagonal of the confusion matrix, indicating the number of pixels classified into their correct ground truth categories. The total number of pixels equals the sum of pixels across all ground truth categories. Overall accuracy is calculated as:

$$OA = (TP + TN) / (TP + FN + FP + TN) \quad (3)$$

The Kappa coefficient is another method for calculating classification accuracy. It is derived by subtracting the sum of the products of the ground truth pixel counts and the classified pixel counts for each category from the product of the total number of pixels (N) and the sum of the diagonal elements of the confusion matrix (X_{kk}), and then dividing by the difference between the square of the total number of pixels and the sum of the products of the ground truth pixel counts and the classified pixel counts for all categories. The Kappa coefficient is calculated as follows:

$$\text{Kappa}=\frac{N\sum_{i=1}^{r} x_{ii}-\sum_{i=1}^{r}(x_{i+}\times x_{+i})}{N^2-\sum_{i=1}^{r}(x_{i+}\times x_{+i})} \quad (4)$$

The classification results for 2023 were validated through field sampling and image screening, with the accuracy as shown in the following Table 4.

Table 4 Classification Accuracy

class	Accuracy	Precision
Forest	0.9107	0.9082
Farmland	0.7599	0.9156
citrus orchard	0.8847	0.8059
Water	0.9953	0.9738
Building	0.8831	0.9401
Bare land	0.8527	0.7537
OA	0.8839	
Kappa	0.8594	

The statistical results of citrus planting areas from 2020 to 2023 were compared with the official statistical yearbook data, and the results are presented in the following Table 5.

Table 5 Comparison of Extracted Areas (2020–2023) with Statistical Yearbook Data

	Statistical Yearbook Data	Extracted Areas	error
2020	14022 hm^2	16257.03 hm^2	15.94%
2021	14784 hm^2	17610.55 hm^2	19.12%
2022	15274 hm^2	14356.91 hm^2	-6.00%
2023	16173 hm^2	15137.23 hm^2	-6.40%

4 CONCLUSION

This study addresses the challenges of large-scale citrus planting area extraction, such as fragmented plots, uneven distribution of ground objects, and diverse vegetation communities. We propose a method combining a deep pyramid-shaped residual network with a decision tree tailored to citrus planting characteristics, achieving citrus planting area identification in southern Jiangxi Province. The key findings are as follows:

(1) The proposed method effectively utilizes spectral and spatial features of multi-spectral image patches, incorporating citrus planting environmental characteristics, such as vegetation coverage, DEM, and illumination shadows for comprehensive evaluation, achieving a classification accuracy of 88%. However, the presence of a small amount of cloud cover in the imagery slightly impacts classification accuracy.

(2) The extraction accuracy of citrus planting areas in Xingguo County, Ganzhou City (2020–2023) was compared with the final statistical yearbook. The results indicate overestimation in 2020 and 2021, primarily due to the misclassification of grasslands and mountains as citrus. In 2022 and 2023, the error was below 6.5%, with an overall estimation accuracy exceeding 80%. This provides a reference for automated monitoring and planting planning of citrus orchards at the county level.

(3) Although the proposed method demonstrates excellent results, several issues remain to be addressed. Our future work will focus on the following two directions. First, we will test multi-spectral imagery from more diverse regions and types to validate the robustness of the method. Second, we will further integrate SAR imagery, such as Sentinel-1, to mitigate the impact of clouds and rain on optical imagery, compensating for the limitations of optical data.

COMPETING INTERESTS

The authors have no relevant financial or non-financial interests to disclose.

FUNDING

The study is supported by the project of Jiangxi Provincial Department of Natural Resources ZRKJ20242501.

REFERENCES

[1] Li SY, Zhou XJ, Yin JM et al. Comprehensive division of climate, topography and soil for navel orange planting in Xunwu County. Acta Agriculturae Jiangxiensis, 2007, 19(5): 40–43.
[2] Xu H, Qi S, Gong P, et al. Long-term monitoring of citrus orchard dynamics using time-series Landsat data: a case study in southern China. International Journal of Remote Sensing, 2018, 39(22): 8271-8292.
[3] Chen Y, Hu J, Cai Z, et al. A phenology-based vegetation index for improving ratoon rice mapping using harmonized Landsat and Sentinel-2 data. Journal of Integrative Agriculture, 2024, 23(4): 1164-1178.
[4] Parente L, Taquary E, Silva A P, et al. Next generation mapping: Combining deep learning, cloud computing, and big remote sensing data. Remote Sensing, 2019, 11(23): 2881.
[5] Tu A, Xie S, Mo M, et al. Water budget components estimation for a mature citrus orchard of southern China based on HYDRUS-1D model. Agricultural Water Management, 2021, 243: 106426.
[6] Xiao C, Li P, Feng Z, et al. Sentinel-2 red-edge spectral indices (RESI) suitability for mapping rubber boom in Luang Namtha Province, northern Lao PDR. International Journal of Applied Earth Observation and Geoinformation, 2020, 93: 102176.
[7] Krizhevsky A, Sutskever I, Hinton G E. ImageNet classification with deep convolutional neural networks. Communications of the ACM, 2017, 60(6): 84-90.
[8] Russakovsky O, Deng J, Su H, et al. Imagenet large scale visual recognition challenge. International journal of computer vision, 2015, 115(3): 211-252.
[9] Zhong Z, Li J, Luo Z, et al. Spectral–spatial residual network for hyperspectral image classification: A 3-D deep learning framework. IEEE transactions on geoscience and remote sensing, 2017, 56(2): 847-858.
[10] Paoletti M E, Haut J M, Fernandez-Beltran R, et al. Deep pyramidal residual networks for spectral–spatial hyperspectral image classification. IEEE Transactions on Geoscience and Remote Sensing, 2018, 57(2): 740-754.
[11] Han D, Kim J. Deep Pyramidal Residual Networks. 2017 IEEE Conference on Computer Vision and Pattern Recognition, 2017: 5927-5935.

Journal of Computer Science and Electrical Engineering
Print ISSN: 2663-1938
Online ISSN: 2663-1946
DOI: https://doi.org/10.61784/jcsee3108

SIMULTANEOUS PLANNING AND DYNAMIC STABILITY SIMULATION VERIFICATION OF HUMANOID ROBOT DANCE MOVEMENTS

JiaXin Huang[1], JunPeng Yuan[1*], Yang Feng[1], XiaoLu Zou[1], YiTing Qiu[1], JingMin Lan[1], Dang Gan[1], LinYing Jiang[1], HaoMin Liang[1], SiNan Ge[2], YuJia Jiang[3]
[1]*School of Mathematics and Information Science, GuangZhou University , GuangZhou 510006, Guangdong, China.*
[2]*School of Computer Science and Network Engineering, GuangZhou University, GuangZhou 510006, Guangdong, China.*
[3]*School of Cyberspace Security, GuangZhou University, GuangZhou 510006, Guangdong, China.*
[*]*Corresponding Author: JunPeng Yuan*

Abstract: This paper addresses the problem of multi-joint trajectory planning and cooperative control for humanoid robots in dance performances. Taking the dance task of the Unitree G1 robot developed by Hangzhou Unitree Robotics at the opening ceremony of a technology exhibition as the background, a hierarchical motion-planning method is proposed that decomposes the overall movement into three sub-tasks: torso rotation, coordinated arm motion, and leg balance adjustment. Torso rotation is planned with a fifth-order polynomial for smooth trajectories; the two arms perform counter-rotating circular motions and their joint angles are computed via inverse kinematics; the legs provide real-time balance compensation based on centroidal dynamics and the Zero-Moment Point (ZMP) stability criterion. Simulation analysis yields coordinated motion trajectories for all 12 degrees of freedom of the torso, arms and legs, achieving fluent dance motions while guaranteeing overall stability and safety during dynamic movement. The study offers a viable theoretical and methodological reference for motion planning and control of humanoid robots in complex scenarios such as artistic performances.
Keyword: Humanoid robot; Trajectory planning; Multi-joint coordination; Inverse kinematics; Stability control; Dance motion

1 INTRODUCTION

With the rapid development of robot technology,humanoid robots, with their anthropomorphic shape and motion capabilities, have shown broad application in many fields such as performing arts, social service, and industrial collaboration[1]. This has made the multi-joint cooperative motion planning and real-time stability control of human robots key technical challenges for achieving their high-level applications[2], which are of great significance for enhancing the expressiveness, safety, and environmental adaptability of the robot's movements.

In terms of robot motion planning problems, existing research has been deeply explored from different dimensions. Researchers have proposed a variety of methods, such as joint space smooth trajectory planning based on polynomials[3] or spline curves[4], and energy-optimal trajectory synchronous planning for industrial scenarios, for redundant or super-redundant robot systems[5], have improved inverse kinematics algorithms and introduced adaptive trajectory tracking and planning strategies[6], to deal with the complexity of kinematic solutions and configuration deviations. In the field of coordinated, the load allocation and joint driving force optimization research of dual-arm robots have provided a theoretical basis for multi-limb collaborative operation[7]. However, the existing research lacks a systematic planning framework for complex artistic movements with multiple degrees of freedom and multiple task couplings under a human-like form, making it difficult for humanoid robots to coordinate the aesthetics movement and achieve real-time balance robustness when executing large-amplitude, dynamic performance movements[8].

This paper takes the dance performance task of Unitree G1 humanoid robot at opening ceremony of the science and technology exhibition as the background, and through the establishment of kinematic and dynamic models, the joint motion trajectory and multi-joint cooperative control of the robot modeled and optimized[9], and the problem of synchronous planning and dynamic stability simulation verification of the whole body coordinated dance movements is studied[10].

2 MODEL CONSTRUCTIONS

2.1 Data Collection and Analysis

In the study of robotic motion planning and control, accurate coordinate transformations from joint space to task space form the foundation for precise motion execution.By analyzing the mapping relationships between the rotational angles of the robot's joint motors and the spatial position of the arm's end-effector, we can not only verify the geometric feasibility of specific motions (such as waving in greeting) but also lay the theoretical groundwork for subsequent trajectory planning, dynamic control, and crucial motor safety validation.

In practical applications, the absence of such calculations would preclude the ability to preemptively determine whether the motors are operating beyond critical parameters—such as torque, rotational speed, and angular range—directly impacting the operational lifespan and safety of the robotic system. Based on this, we conducted data collection, and Table 1 presents some parameters of the robot working normally and running stably.

Table 1 Summary of Collected Robot Parameters

Metric	Parameter
Dimensions (Standing)	1320x450x200mm
Dimensions (Folded)	690x450x300mm
Total Degrees of Freedom (DoF)	23-43
Maximum Knee Joint Torque	120N·m
Maximum Arm Payload	Approx. 3 kg
Lower Leg + Thigh Length	0.6m
Intelligent Battery Capacity	9000mAh
Charger (Quick-Release)	54V 5A
Extended Joint Range of Motion	Waist Joint:Z±155°、X±45°、Y±30° Knee Joint:0~165° Hip Joint:P±154°、R-30~±170°、Y±158 Wrist Joint:P±92.5°、Y±92.5°

For this study, the robot is required to perform a 45° leftward body rotation while simultaneously moving both arms in circular motions about the shoulders. The circular path has a radius of 300 mm and a period of 4 seconds, with the two arms moving in opposite directions. To maintain balance during this motion, the legs must be adjusted accordingly. A mathematical model needs to be established to describe how the joint angles of both arms and legs vary with time t ($0 \leq t \leq 4$).

2.2 Framework for Decomposition and Modeling of Complex Motor Tasks

To achieve precise planning of this compound motion, we first decompose it into three relatively independent yet interconnected subtasks:
Trunk rotation task: Control the waist joint to achieve a smooth 45° yaw rotation.
Bimanual cooperative task: Plan circular trajectories for the left arm (counterclockwise) and the right arm (clockwise) separately.
Leg balancing task: Adjusting leg posture in real time according to upper body movement to ensure stable center of gravity.
Meanwhile, we establish a unified time reference and local spatial coordinate systems, define the total motion duration as T = 4 s, and introduce a normalized time variable to simplify the trajectory functions. Spatially, we set up local coordinate systems for the torso, arms, and legs separately to facilitate the description of relative motions of each body part.

2.3 Smooth Rotational Motion Trajectory Planning of the Trunk Based on Quintic Polynomials

To avoid impacts on the motor during startup and shutdown, we continue to use a quintic polynomial for trajectory planning of the trunk's rotational motion, ensuring continuity in angle, angular velocity, and angular acceleration. The solution derived from Problem 2: (a quintic polynomial odd function satisfying smoothness conditions):

$$p(\tau)=10\tau^3-15\tau^4+6\tau^5 \tag{1}$$

The trunk rotation angle function is defined as:

$$\theta_{torso}(t)=45^\circ \cdot p(\tau)=45^\circ \cdot p\left(\frac{t}{4}\right) \tag{2}$$

By differentiating the angular function, the angular velocity and angular acceleration of trunk rotation can be obtained, which are key parameters for subsequent dynamic analysis and motor load evaluation.

$$\omega_{torso}(t)=\frac{d\theta_{torso}}{dt}=\frac{45^\circ}{4} \cdot p'(\tau) \tag{3}$$

$$\alpha_{torso}(t)=\frac{d^2\theta_{torso}}{dt^2}=\frac{45^\circ}{16} \cdot p''(\tau) \tag{4}$$

Among them, $(\tau)=30\tau^2-60\tau^3+30\tau^4$, $p''(\tau)=60\tau-180\tau^2+120\tau^3$.

2.4 Modeling of Dual-Arm Cooperative Circular Motion Based on Inverse Kinematics

The motion trajectories of the end points of the two arms in their respective shoulder joint coordinate systems are described by circular parametric equations. The circular radius is set as R = 0.3 m, and the angular frequency of motion is $\omega = 2\pi$ rad/s.
Left arm (counterclockwise) trajectory:

$$\begin{cases} x_L(t)=R\cdot\cos(\omega t) \\ y_L(t)=R\cdot\sin(\omega t) \\ z_L(t)=0 \end{cases} \tag{5}$$

Right arm (clockwise) trajectory:

$$\begin{cases} x_R(t)=R\cdot\cos(\omega t+\pi) \\ y_R(t)=-R\cdot\sin(\omega t+\pi) \\ z_R(t)=0 \end{cases} \tag{6}$$

Given the position of the end point, the required shoulder joint angles for actuation are determined through inverse kinematics. The shoulder joint yaw angle determines the arm's orientation in the horizontal plane.

$$\theta^{L}_{shoulder\_yaw}(t)=\arctan\left(\frac{y_L}{x_L}\right)=\arctan\left(\frac{R\sin(\omega t)}{R\cos(\omega t)}\right)=\omega t \tag{7}$$

$$\theta^{R}_{shoulder-yaw}(t)=\arctan\left(\frac{y_R}{x_R}\right)=\arctan\left(\frac{-R\sin(\omega t+\pi)}{R\cos(\omega t+\pi)}\right)=\omega t+\pi \tag{8}$$

Since the motion occurs in the horizontal plane, the shoulder joint pitch angle remains at 0 throughout this task.

Model the arm as a two-link mechanism consisting of an upper arm (L1 = 0.2 m) and a forearm (L2= 0.15 m). The elbow joint angle θelbow is determined using the law of cosines to maintain a constant distance R between the end point and the shoulder.

$$\theta_{elbow}(t)=\arccos\left(\frac{L_1^2+L_2^2-\|\vec{P}_{end}\|^2}{2L_1L_2}\right) \tag{9}$$

This angle remains constant during the motion.

2.5 Leg Balance Control Based on Center of Mass Stability

The robot's overall center of mass (CoM) position is central to balance control. The total CoM is calculated by summing the centers of mass of individual components, taking into account their respective masses and real-time positions.

$$CoM_x(t)=\frac{\sum m_i x_i(t)}{\sum m_i} \tag{10}$$

$$CoM_y(t)=\frac{\sum m_i y_i(t)}{\sum m_i} \tag{11}$$

Where,mi and (xi(t),yi(t)) are the masses and the coordinates of the centers of masses of the trunk, arms, and legs respectively.

The stability region of a robot is defined by the support polygon formed by the contact points of its two feet with the ground. The key to determining whether the robot is stable lies in whether its zero moment point (ZMP) always projects within the support polygon. The formula for calculating ZMP is:

$$ZMP_x(t)=CoM_x(t)-\frac{CoM_z\cdot\ddot{CoM}_x(t)}{g} \tag{12}$$

$$ZMP_y(t)=CoM_y(t)-\frac{CoM_z\cdot\ddot{CoM}_y(t)}{g} \tag{13}$$

To counteract disturbances to the center of mass caused by upper body motion, leg joints need real-time compensation.

① Hip joint compensation: generating movement in the opposite direction of trunk rotation to counteract inertia.

$$\theta^{L}_{hip}(t)=k_{hip}\cdot\theta_{torso}(t),\ (k_{hip}<0) \tag{14}$$

② Ankle joint compensation: Proportional control based on the deviation of the center of mass in the Y direction, rapidly adjusting the support base.

$$\theta_{ankle}(t)=k_{ankle}\cdot(CoM_y(t)-CoM_{y,target}) \tag{15}$$

③ Knee joint: Maintain a slight 5° flexion to enhance postural elasticity and shock absorption.

2.6 Constructions and Solution to Model

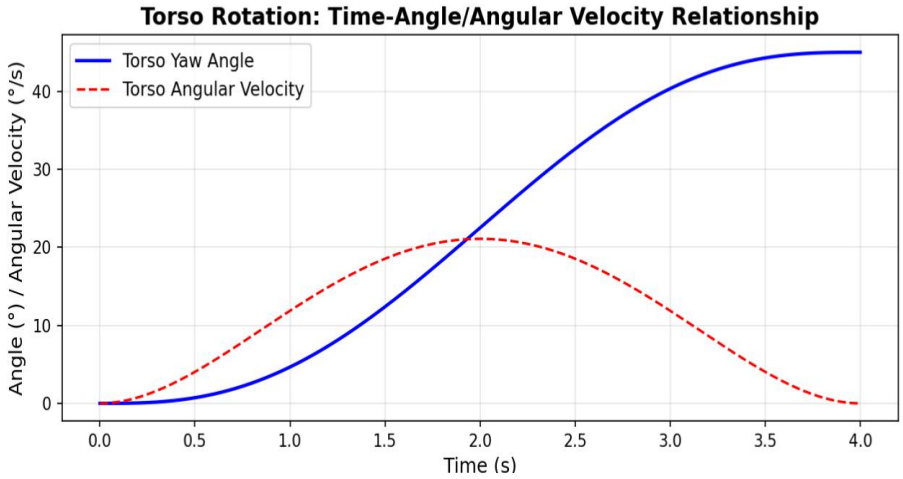

Figure 1 Time-Angle Velocity Relationship

The Figure 1 shows the curves of trunk pitch angle and angular velocity varying with time. Over the entire 4-second performance period, the robot's waist completes a left turn from 0° to 45° along a smooth fifth-order polynomial trajectory. The angle curve is continuous without noticeable inflection points or abrupt changes, and the corresponding angular velocity exhibits a symmetric bell-shaped distribution. The peak angular velocity is only 21°/s, significantly below the safety threshold of 3 rad/s, ensuring an elegant on-stage turn while avoiding impact on joint motors during startup and braking. Meanwhile, the maximum angular velocity occurs at t = 2 s, aligning with the midpoint of the circular motion of the arms, thereby maintaining rhythmic synchronization among upper body movements and providing a stable, disturbance-free postural reference for subsequent coordinated control of the arms and lower limbs.

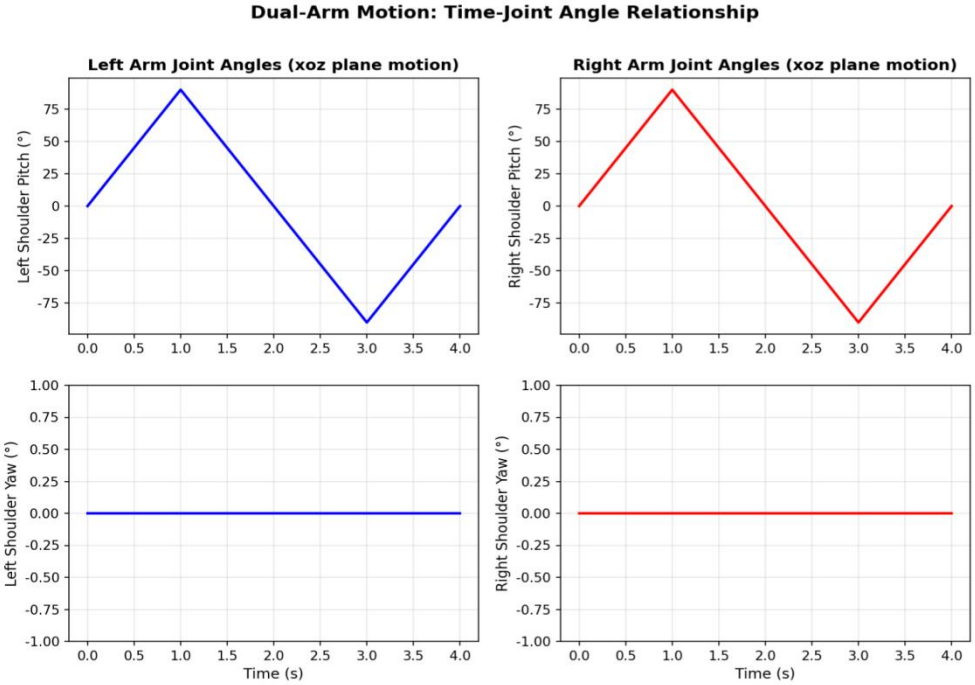

Figure 2 Dual-Arm Motion: Time-joint Angle Relationship

The above Figure 2 presents the curve of the left and right joint angles changing over time in the dual-arm motion..Two sinusoidal trajectories with a 180° phase difference are clearly visible, oscillating uniformly within a range of ±75°, each completing one full circular motion within four seconds, demonstrating a perfect mirror-image reversal effect. The angular velocity remains constant at 90°/s—less than 1.6 rad/s after conversion—only half of the motor's safe limit, with smooth curves free of sharp peaks. This indicates that the quintic polynomial interpolation not only accurately realizes the planned angular trajectory but also keeps both velocity and acceleration within comfortable ranges, ensuring balanced motor loading, controlled temperature rise, and enabling the robot to perform a natural, fluid dance movement of "alternating circular motions with both hands".

Table 2 Angular data from the perspective of key moments

moment/s	1.0	2.0	3.0	4.0

Trunk pitch angle(°)	4.66	22.50	40.34	45.00

The trunk pitch angle data of the key moment of the robot motion are recorded in the Table 2.

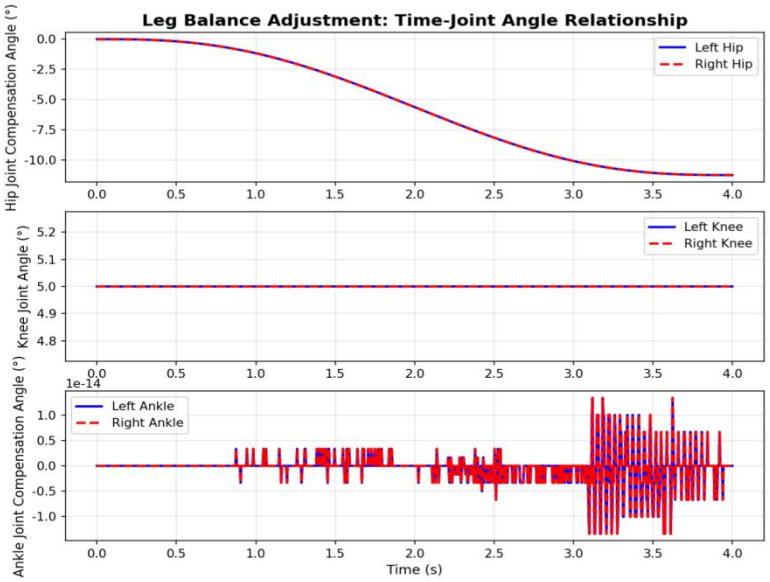

Figure 3 Leg Balance Adustment: Time-joint Angle Relationship

The Figure 3 shows real-time adjustment curves of lower-limb balance joints: the hip joint gradually returns from −11.25° to 0° through a counter-rotation strategy, counteracting the angular momentum generated by trunk rotation to the left; the ankle joint makes high-frequency fine adjustments within ±1°, quickly compensating for lateral shifts in center of mass; the knee joint remains constantly flexed at 5°, providing vertical elastic buffering for the entire system. Although the amplitudes of these three curves are small, their phases are strictly synchronized with trunk motion, successfully bringing the projection of the upper body's center of mass back to the center between both feet. This enables the robot to maintain upright stability without any stepping movement within four seconds, embodying the control philosophy of "dynamic upper body, stable lower body."

3 MODEL STRENGTHS AND EXTENSIONS

3.1 Strengths

1.Effective simulation validation with intuitive parameter visualization: Numerical simulations produced time-varying joint-angle curves for all twelve planned degrees of freedom, supplemented by data tables at key instants. The plots and numbers clearly demonstrate the smoothness and synchrony of every joint motion as well as the balance-compensation effect, providing direct and compelling evidence for the validity of the theoretical model.
2.Hierarchical and modular modeling with clear structure: The complex whole-body dance motion is decomposed into three relatively independent yet interrelated sub-tasks—torso rotation, coordinated arm motion, and leg balancing—within a unified temporal and spatial reference frame. This layered, modular design reduces the complexity of coordinating a multi-DOF system and enhances the model’s interpretability and maintainability.

3.2 Extensions

1. Extended application scenarios: The cooperative-planning and balance-control framework developed for dance performances can be readily extended to additional humanoid-robot applications—such as gesture guidance and posture adjustment in reception services, load-handling and obstacle-avoidance tasks in industrial settings, or even compliant assistance motions in rehabilitation training—by simply retuning trajectory parameters and constraint conditions to suit each specific task.
2. Enhanced platform adaptability: The core ideas of hierarchical planning, polynomial-/IK-based trajectory generation, and ZMP-driven stability compensation are inherently generic. Follow-up work can adapt these modules to humanoid or biomimetic platforms with varied kinematic configurations (different DOF layouts, mass parameters, etc.), yielding a universal dynamic-motion-planning toolchain.

4 CONCLUSIONS

This paper focuses on the multi-joint coordinated motion planning and dynamic stability control problems of humanoid robots in dance performance scenarios, carries out systematic modeling and simulation research. Taking the dance

action of "turning the trunk 45° to the left with the double arms in reverse circular motion" completed by Unitree G1 robot as an example, a hierarchical and modular motion planning framework is proposed. This framework decouples the complex whole-body motion into three sub-tasks: trunk, dual-arm coordination, and leg balancing, and models and controls them respectively using quintic polynomials, inverse kinematics, and real-time compensation strategies based on the center of massCoM) and zero moment point (ZMP).

Through numerical simulation, a smooth and synchronized joint motion trajectory covering 12 degrees of freedom of the trunk, arms, and both legs was successfully generated. The results show that the designed trajectory can ensure that the angular velocity and acceleration of each joint are always within the safe threshold, effectively motor impact. At the same time, the model-based leg compensation mechanism can respond to the disturbances brought by the upper body motion in real time, making the ZMP always inside the supporting polygon, thereby maintaining the overall upright stability of the robot during the four-second dynamic performance without the need to adjust steps. This verifies the effectiveness of the " body moves, lower body stable" control concept in achieving dynamic artistic expression.

This research not only provides a feasible planning and control solution for specific dance movements, but also provides theoretical and methodological references for safe and smooth motion control of humanoid robots in other complex dynamic scenarios (such as service interaction, industrial operation).

COMPETING INTERESTS

The authors have no relevant financial or non-financial interests to disclose.

REFERENCES

[1] Chijioke Leonard Nkwocha, Adeayo Adewumi, Samuel Oluwadare Folorunsho, et al. A Comprehensive Review of Sensing, Control, and Networking in Agricultural Robots: From Perception to Coordination. Robotics, 2025, 14(11).

[2] Vahid Mohammadi, Mojtaba Hosseini, Farhad Jafari, et al. RoboMan: An Adult-Sized Humanoid Robot with Enhanced Performance, Inherent Stability, and Two-Stage Balance Control to Facilitate Research on Humanoids. Robotics, 2024, 13(10).

[3] Zhang Yu, Yu Yang, Wang Wenxue, et al. Trajectory planning of parallel mechanism based on mixed polynomials. Computer Simulation, 2025, 42(09): 477-482+514.

[4] Yiqin Luo. A Space Discretization Method for Smooth Trajectory Planning of a 5PUS-RPUR Parallel Robot. Applied Sciences, 2025, 15(6): 9212-9212. DOI: 10.3390/APP15169212.

[5] Luo Shuangbao, Zeng Fengfei, Zeng Xiaosan, et al. Research Adaptive Motion Planning Method for Multi-joint Hyper-redundant Robot. Mechanical Transmission, 2024, 48(08): 6-32.

[6] Yanan Qin, Qi Chen. Trajectory planning and tracking control for cable-driven continuum robots with dynamic obstacles. Journal of the Franklin Institute, 2025, 362(16).

[7] Zhou Haibo. Design of composite joint leg structure and its elastic motion research for reconfigurable biped robots. Shanghai, 2024. DOI: 10.27300/d.cnki.gshau.2024.00041.

[8] Di Zhou, Jinrui Han, Zhen Chen, et al. Dynamic reliability assessment for motion stability of industrial robot based on high-order response moments. Measurement, 2025, 246.

[9] Wang Tingting. Research on Optimal Control Methods for Joint Motors of Robotic Arms. Changchun University of Technology, 2023. DOI: 10.27805/d.cnki.gccgy.2023.00002.

[10] Zhang Shichao, Liu Zhaobiao, Zhu Yuquan, et al. Kinematic Analysis and Simulation of a Sixaxis Robot Based on CoppeliaSim. Journal of Shipboard Electronics and Countermeasures, 2025, 48(05): 100-104+120. DOI: 10.16426/j.cnki.jcdzdk.205.05.020.

Journal of Computer Science and Electrical Engineering
Print ISSN: 2663-1938
Online ISSN: 2663-1946
DOI: https://doi.org/10.61784/jcsee3106

VISUALIZATION PLATFORM FOR OCEAN ACOUSTIC SIMULATION BASED ON MAYAVI

Yan Zhang
School of Artificial Intelligence and Computer Science, North China University of Technology, Beijing 100144, China.

Abstract: Meteorological navigation data are critical to navigational safety and route planning, but their massive volume imposes a heavy burden on data storage and communication in intelligent shipping systems. Considering the spatiotemporal characteristics of such data and the fact that they allow lossy compression within an acceptable error range, this paper proposes an efficient error-guaranteed lossy compression method for floating-point data. The method modifies the binary representation of mantissa bits within a preset error bound to increase the number of trailing zeros in the XOR results between adjacent values, thereby reducing the meaningful bits that need to be encoded, and selects corresponding encoding strategies according to the resulting XOR patterns. Experimental results on public datasets and real meteorological navigation datasets show that, compared with existing mainstream compression algorithms, the proposed method incurs slightly higher compression time but achieves the highest compression efficiency under the preset error constraints, demonstrating its suitability for scenarios with strict error control requirements in large-scale meteorological navigation data storage and transmission.
Keywords: Mayavi; Volume rendering; Ocean acoustics; Data visualization

1 INTRODUCTION

Underwater detection and communication systems are key components in marine engineering and scientific research, widely used for tasks such as underwater target detection, seabed communication, and marine environmental monitoring. The practical application environments of these systems often face challenges such as complex hydrological conditions, high-cost equipment investment, and uncontrollable risks. In this context, the proposal of a simulation visualization platform becomes an important breakthrough to address these issues. By constructing underwater environment simulation visualization models, users can simulate the acoustic propagation characteristics of real oceans within virtual scenarios. The introduction of simulation technology essentially provides an efficient and controllable platform to overcome the constraints of underwater environments and accelerate the pace of technological development.

Marine acoustics visualization is a research field that transforms marine basic data and ocean acoustic field data into multidimensional dynamic visual images based on the physical laws of acoustics, combined with data modeling and graphics rendering techniques. However, the spatial and temporal variations in water density, temperature, and salinity in underwater environments make the process of sound wave propagation extremely complex, posing significant challenges for visualization simulations. Currently, as society's demand for marine simulations continues to grow, higher requirements are placed on the design and performance of system platforms. To meet social needs and promote the continuous development of marine detection technologies, there is a need to develop a simulation visualization platform. Traditional acoustic field calculation models are limited by single-thread computing modes, resulting in low efficiency and long processing times in scenarios requiring simultaneous multi-angle acoustic field solutions in complex marine environments. In ship navigation scenarios, it is necessary to achieve minute-level response times to support real-time decision-making. Additionally, the platform should adopt a modular architecture design and real-time human-machine interaction mechanisms to create a user-friendly system that aligns with operational workflows.

Therefore, by integrating the Mayavi 3D visualization engine, GIS electronic maps, and parallelized acoustic field calculation models, an efficient and highly interactive marine acoustics simulation visualization platform has been constructed. This platform provides visual decision support for marine acoustics modeling and scientific research validation, possessing significant engineering application value.

2 RELATED WORK

With the growing exploitation of marine resources and increasing global demand for maritime security, underwater detection has become increasingly vital in national defense, marine engineering, and scientific research. As a key research focus in ocean acoustics, underwater acoustic field simulation and visualization has been widely applied in marine exploration, environmental monitoring, and underwater communication, achieving significant technological advancements in recent years.

Internationally, the ray theory established by C S Clay and H Medwin in the 1970s laid the foundation for the study of underwater acoustic propagation. The University of Texas at Austin[1] developed the SEA (Simulation Environment for Acoustics) underwater acoustic simulation tool, which enables high-precision modeling of sound wave propagation

characteristics in complex marine media. Michael B. Porter[2] developed the Bellhop acoustic model, which effectively mitigates inaccuracies of traditional models in caustic and shadow zones by integrating the advantages of ray tracing and wave-theoretic approaches. Furthermore, the Underwater Acoustics Technical Committee of the Acoustical Society of America[3] has improved target recognition accuracy in complex environments through multi-sensor data fusion and intelligent algorithms. The University of Tokyo[4] developed Kraken, an underwater acoustic simulation model based on normal mode theory. Kraken effectively simulates underwater sound propagation and scattering phenomena and is typically employed for horizontally stratified media where environmental properties are independent of horizontal range.

Domestically, significant progress has also been made in underwater acoustic field simulation technologies.Yang Jiaxuan et al.[5] utilized the Bellhop model to simulate sound propagation over varying seabed topographies, investigating the influence of seafloor terrain on acoustic transmission.In 2018, Chen Xinning et al.[6] proposed a RAM (Range-Dependent Acoustic Model)-based simulation method for ocean acoustic channel impulse responses, aiming to address the high computational complexity associated with real-time broadband signal simulation involving multiple sensors and targets. Li Meng et al.[7] applied the Bellhop model to simulate underwater acoustic channels and explored detection methods for target sources as well as the relationship between optimal hydrophone array deployment and ray paths. In 2020, Wang Siqi[8] developed an underwater acoustic field simulation system based on the Bellhop model. Additionally, Li Zheng et al.[9] designed and implemented a six-element ocean acoustic positioning simulation system using the MATLAB/Simulink platform, overcoming the high cost and limited flexibility of traditional hardware-dependent acoustic positioning systems.

Scientific visualization originated from computer graphics in the 1960s and was initially used for simple two-dimensional graphical representations. William Lorensen pioneered the Marching Cubes algorithm, which sparked widespread interest in scientific visualization. Numerous algorithms have since been developed to implement volume rendering techniques. Markus and Ljung[10] proposed an image-space ray casting method that enabled global visualization of three-dimensional scalar fields. Tian Liang et al.[11] introduced a footprint-based method in object space and leveraged CUDA parallel computing to optimize this approach, effectively overcoming the limitations of traditional algorithms—namely, high computational cost and low efficiency. Lacroute[12] developed an efficient volume rendering technique based on shear-warp factorization of the view transformation.

3 SYSTEM DESIGN

This paper presents the design and development of a marine acoustics simulation and visualization platform based on Mayavi. The platform is designed to enable three-dimensional visualization of simulated marine acoustic data, thereby providing robust visual support for acoustic field modeling and scientific validation in complex marine environments. Employing a modular architecture, the platform facilitates the extension and updating of its acoustic model library, offering a scalable and extensible technical verification environment for marine acoustics research.

3.1 Architecture of the Marine Acoustics Visualization System

The marine acoustics visualization platform is primarily based on a five-layer architectural design. The architecture of the visualization system is illustrated in Figure 1.

The Application Layer resides at the top of the system architecture and is primarily responsible for handling business logic, functional implementation, and user interaction. It directly responds to business requirements by invoking lower-level services such as the data layer and interface layer to accomplish specific tasks. Its main functions encompass GIS-based route planning, environmental data visualization, and sound propagation data visualization.

The Component Layer achieves high cohesion and low coupling design objectives by decomposing the system into independent functional components. It consists of multiple functional components, primarily including: The 2D Plotting Component is primarily used for interactive display on GIS maps, including content such as propagation loss plan views, propagation loss profile plots, and sound ray trajectory profile plots. It can dynamically display user-required information on the map by employing different 2D visualization techniques tailored to various data types. The 3D Plotting Component supports sound field volume rendering, 3D terrain visualization, and 3D data slicing. It can dynamically display three-dimensional effects of the marine environment based on user interaction, serving to assist the display and interactive control of the main view. The Sound Field Calculation Component enables single-bearing and multi-bearing propagation loss calculations by invoking sound field calculation models. It also supports data interpolation of the calculation results to enhance the smoothness and continuity of subsequent visualizations.

The visualization engine layer serves as the core architectural tier of the visualization system, bearing the crucial functions of data transformation and graphical rendering. This platform achieves efficient rendering by leveraging underlying graphics libraries such as HTML, Mayavi, QcustomPlot and Echarts, supporting both 2D and 3D graphics. Built-in chart components within the libraries include bar charts, scatter plots, heatmaps, topology diagrams, maps, among others, and also support custom component development to meet the requirements of specialized scenarios[13]. It concurrently supports user interactions (such as zooming, dragging, clicking, and box-selecting) and triggers corresponding events—for example, drawing flight routes within a GIS or clicking on a waypoint to display detailed information. During user interaction, the system enables dynamic effects like animated transitions and highlight linkage, thereby enhancing the user experience.

The Interface Layer serves as the central hub for system function orchestration and is designed with three standardized functional modules:

1.Data Management Interface: Provides unified access and management capabilities for multi-source, heterogeneous marine environmental data. It supports the standardized import and dynamic loading of professional data, including terrain profiles, sound speed profiles, seabed sediment parameters, and more.

2.Data Query Interface: Enables querying of various marine data types from marine databases or local .nc (NetCDF) files.

3.Acoustic Field Calculation Interface: Integrates the Bellhop ray-tracing model and the RAM parabolic equation model based on Dynamic Link Library (DLL) technology. Through a parameterized invocation mechanism, it supports calculations for single-azimuth acoustic ray propagation paths and multi-azimuth acoustic field coverage, including propagation loss.

This hierarchical interface architecture ensures module independence while achieving a balance between functional extensibility and computational efficiency for marine environmental data processing, acoustic model computation, and visual representation.

The Data Layer is primarily responsible for integrating and managing multi-dimensional marine environmental data, which mainly consists of four major categories: seabed topographic and geomorphic data, seabed sediment type distribution data, sound speed profile characteristic data, and acoustic field calculation model data. The data primarily originates from publicly available datasets, with the platform acquiring it through external interfaces or by reading local files.

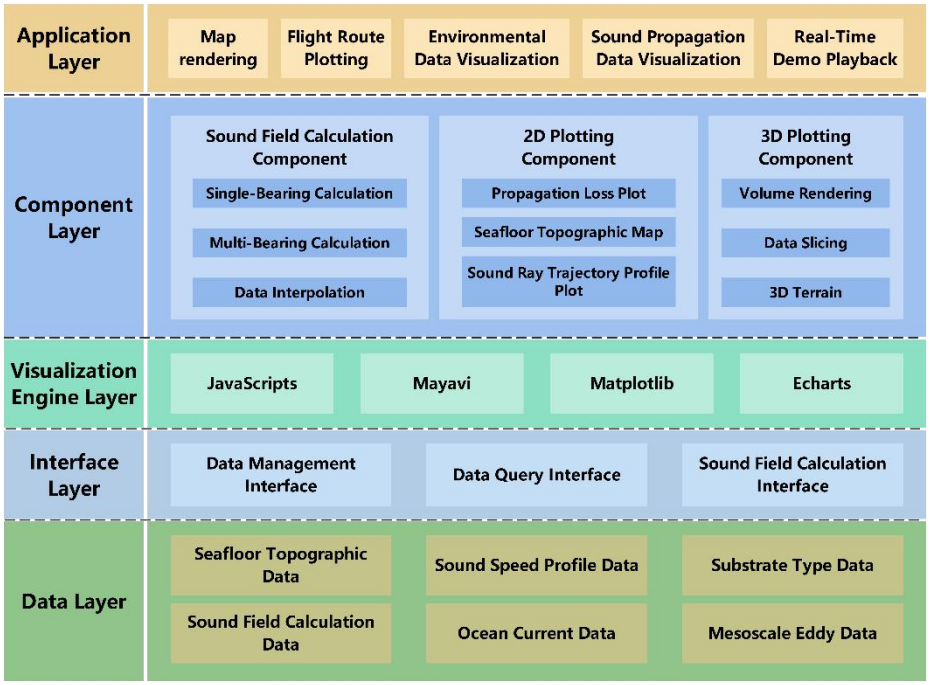

Figure 1 Visualization System Architecture

3.2 Core Function Design

The marine acoustics simulation visualization platform, based on a modular architecture design, implements a complete workflow encompassing marine environmental data integration, acoustic field computation, and interactive visual analysis. The system's functional design covers five core modules (GIS Map Management, Acoustic Field Calculation Management, Environmental Data Management, Environmental Data Visualization, and Acoustic Propagation Data Visualization). These modules are realized through a layered architecture consisting of the Application Layer, Component Layer, Visualization Engine Layer, Interface Layer, and Data Layer, achieving functional decoupling and coordinated operation. The specific functional structure is illustrated in Figure 2.

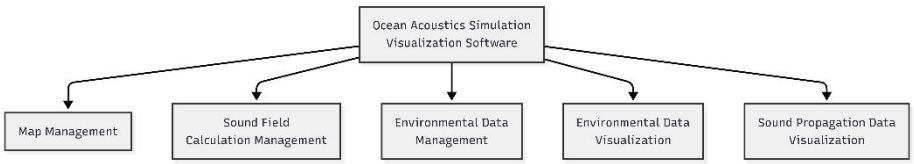

Figure 2 EGFC Encoding Strategy

3.2.1 GIS map management

Map rendering is based on HTML5 front-end technology, utilizing tile data splicing to achieve dynamic map drawing. Tile data is sourced from public TMS tile servers. The acquired target area data is compatible with the Web Mercator projection in Google Earth tile format. By adjusting the Y-axis numbering direction, the data is converted to the OpenStreetMap standard tile structure. The system then uses the PyQt5 QWebEngineView component to load a local Leaflet map page, enabling tile data visualization. JavaScript interaction logic is integrated into the GIS map, supporting latitude-longitude coordinate-based point markers, polyline drawing, and polygon area plotting through coordinate conversion and Leaflet drawing interfaces. The system also includes ship route dynamic simulation functionality. The GIS map is illustrated in Figure 3.

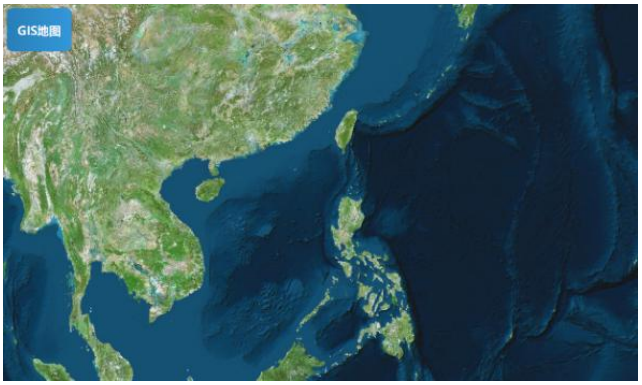

Figure 3 Functional Module Design

3.2.2 Acoustic field calculation management

Acoustic field calculation management supports the import of different acoustic models for computation. Currently, it accommodates the parabolic equation model (RAM) and the Gaussian beam ray model (Bellhop)[14]. The models require loading marine environmental data, including seabed topography data, sediment type data, and sound speed profile data, along with input parameters (such as frequency, step size, number of azimuths, etc.) to generate acoustic propagation loss field distribution results.

To address the computational efficiency bottleneck of traditional acoustic field models, a multi-core CPU parallel acceleration approach is adopted, optimizing the serial iterative computation mode into a multi-threaded parallel computation scheme[15]. The acoustic field calculation service employs a process-level parallel acceleration strategy: for each request, an independent process is dynamically created to fully utilize multi-core CPU resources. Furthermore, to further enhance performance, thread-level parallel technology is implemented in conjunction with a CPU affinity mechanism. This mechanism binds specific threads to designated physical CPU cores, allowing them exclusive access to core resources. This binding offers dual advantages: first, it minimizes thread context switching overhead; second, it prevents the operating system from dynamically scheduling threads across different cores, thereby significantly improving CPU cache hit rates. Together, these measures effectively boost overall computational performance.

By pooling CPU computing resources, computational efficiency is further enhanced. The acoustic field calculation service can allocate required resources from the resource pool on demand and, combined with computational caching techniques, achieves high-performance data processing. This approach maximizes the utilization of hardware resources.

3.2.3 Environmental data management

Environmental data encompass multiple marine environmental elements, including seabed topography, sediment types, sound speed profiles, ocean currents, and mesoscale eddies. In the data processing workflow, raw data are stored locally in two standardized file formats: .nc (NetCDF format) and .tif (geographic raster format), and are integrated and parsed through the visualization platform. The NetCDF4 library is utilized to read multidimensional scientific datasets in .nc format, while the GDAL library is employed to parse geographic spatial raster data in .tif format. After parsing, both types of data are uniformly converted into the NumPy array format. Leveraging the robust multidimensional array processing capabilities of the NumPy library, preprocessing operations such as data format standardization, spatial interpolation, and 3D data reconstruction are performed, providing standardized data support for subsequent visualization rendering and spatial analysis.

3.2.4 Environmental data visualization

This module adopts a multi-source data fusion architecture, integrating three foundational layers: Geographic Information System, seabed topography, and seabed sediment properties. The system presents GIS and sediment attribute information in the form of a two-dimensional planar base layer, while simultaneously rendering terrain data in three dimensions to construct a spatially depth-aware topographic model.

For three-dimensional terrain modeling, volume rendering is implemented based on the Mayavi scientific visualization engine. The core technique employs the ray casting algorithm combined with transfer functions for data mapping. The fundamental principle of ray casting involves projecting rays from the viewpoint through the outermost pixels of the image sequence and across the volume data. During this process, the volume data is sampled at intervals. Transfer functions are then applied to assign color and opacity values to each sampling point. Based on a lighting model, these

values are accumulated along a fixed direction until the ray traverses the entire volume dataset. The final synthesized opacity and color values correspond to the opacity and color of the pixel projected onto the screen.

The lighting model employed in the ray casting method is the Phong illumination model. Its principle treats ambient light as a constant, and when an object's surface is illuminated by a light source, the reflected light includes not only ambient and diffuse components but also specular reflection[16]. Once the ambient light intensity and the material's specular reflection coefficient are determined, the intensity of the reflected light ultimately perceived by the human eye is related to two angles: one is the angle θ between the incident light direction and the surface normal of the object, and the other is the angle γ between the viewing direction and the reflected light direction. The Phong illumination model can be expressed by Equation 1:

$$I_d=k_a I_a+k_d I_s \cos\theta+k_s I_s(\cos\gamma)^n \quad (1)$$

Where k_s represents the material's specular reflection coefficient, denotes the light intensity from the ambient light component interaction, indicates the light intensity from the diffuse reflection component interaction, is the specular exponent reflecting the surface glossiness of the material, and expresses the light intensity from the specular reflection component interaction.

Furthermore, the system provides interactive visualization controls, allowing users to dynamically switch between two-dimensional planar mode and three-dimensional stereoscopic mode. The three-dimensional view supports 6-degree-of-freedom spatial rotation operations.

For marine current vector field data, the system implements a hybrid 2D/3D visualization scheme. It can present the flow field as a two-dimensional planar vector diagram and also construct a three-dimensional spatial streamline model for ocean currents (as illustrated in Figure 4).

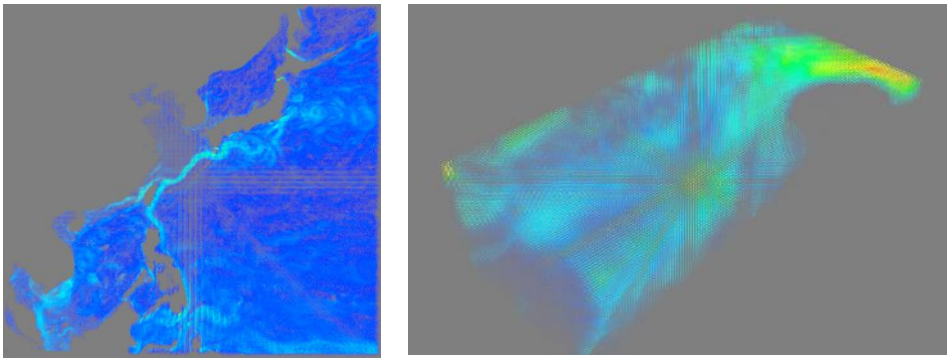

Figure 4 2D Ocean Current and 3D Ocean Current

3.2.5 Acoustic propagation data visualization

For acoustic wave propagation attenuation data obtained from numerical simulations of acoustic field models, multidimensional visualization techniques are employed to spatially represent acoustic field characteristics, including top-down views, profile views, and three-dimensional acoustic field volume rendering.

The 3D acoustic field volume rendering system provides multi-axis slice analysis functionality, supporting three-dimensional orthogonal cross-section operations based on the Cartesian coordinate system. Users can examine acoustic field cross-sections at any depth or select specific angles to obtain attenuation characteristic maps of acoustic fields in particular propagation directions.

To meet the requirements for top-down visualization of acoustic field propagation loss, a segmented linear interpolation method is applied based on discrete azimuth angle data (distributed in eight or sixteen sector divisions) output by the acoustic field model. This method generates continuous acoustic field distributions between adjacent sector boundaries—interpolation is performed every 22.5° for 16-sector data and every 45° for 8-sector data—resulting in a complete acoustic field dataset comprising 360 data points at 1° intervals.

A jet colormap is adopted, with the propagation loss intensity range fixed within [40, 120] dB, This ensures that outliers do not cause chromatic shift in the color scale. A nonlinear color mapping rule is established:

(1) High-intensity regions (≥100 dB) are mapped to dark blue hues;

(2) Medium-intensity regions (70-100 dB) transition through cyan to yellow hues;

(3) Low-intensity regions (≤70 dB) are consistently displayed in red hues.

4 SYSTEM APPLICATION EXAMPLES

4.1 Data Import

The tile map service based on the Leaflet framework must strictly adhere to OpenStreetMap standard specifications, including elements such as zoom levels, coordinate projections, and tile naming conventions. The submarine foundational geographic data layer (including substrate classification, seabed terrain models, and three-dimensional environmental feature data) requires spatial data storage in GeoTIFF format. For the marine dynamic environment data, ocean current field information must be provided in NetCDF format. All data should possess complete spatial reference

system definitions and metadata descriptions to ensure spatiotemporal alignment and system compatibility among multi-source heterogeneous data.

4.2 Model Calculation

This platform integrates both the Bellhop and RAM underwater acoustic propagation models. Users can perform real-time acoustic field simulation calculations for designated sea areas through a visual interface by invoking the acoustic field calculation model to compute propagation loss values at selected locations.

The fundamental principle of the Bellhop model is briefly introduced below. Bellhop calculates the acoustic field in horizontally inhomogeneous environments using the Gaussian Beam Tracing method. The core idea of this method is to assign a Gaussian intensity distribution to each acoustic ray (i.e., the beam centerline). These rays can transition smoothly into shadow zones and pass through caustics with minimal discontinuity, yielding results that more closely approximate wave theory. The central formula of Bellhop is the Gaussian beam acoustic pressure field expression:

$$u(s,n)=A\sqrt{\frac{c(s)}{rq(s)}}\exp(-iw[\tau(s)+\frac{1}{2}\frac{p(s)}{q(s)}n^2]) \tag{2}$$

Where A is an arbitrary constant, $c(s)$ is the sound speed along the ray as a function of arc length s, r is the horizontal range, $q(s)$ is the complex beam curvature parameter, $p(s)$ is the complex beam width parameter, $\tau(s)$ is the travel time integral along the ray, ω is the angular frequency of the sound source, n is the distance perpendicular to the central ray. The interface for acoustic field model calculation is shown in Figure 5.

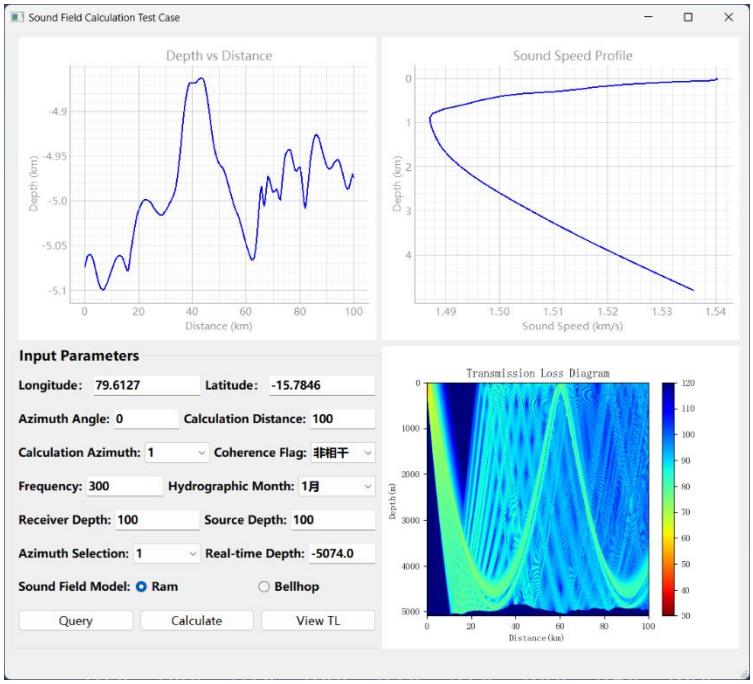

Figure 5 Propagation Loss Calculation in Acoustic Field Models

4.3 Result Visualization

The main interface of the Marine Acoustics Visualization Platform features a GIS map. Within the marine environment scenario, users can load a global marine GIS map through the platform's main interface to quickly locate target sea areas. The GIS map also supports functionalities such as point marking, area plotting, and symbolic annotation to aid in decision-making. Users can obtain marine environmental data for the specified area—including substrate type, sound speed profile, and seabed topography—and render this data in both two-dimensional and three-dimensional forms for visualization. These data simultaneously provide fundamental environmental parameters for subsequent acoustic field calculations.

During the acoustic field model calculation phase, the platform imports the marine environmental data into its built-in acoustic field models for parallel computation, generating acoustic propagation data for the target location. Users can analyze the acoustic propagation loss in the area by selecting from various visualization formats, such as plan view, profile view, and three-dimensional acoustic field volume rendering. As shown in Figure 6, the left side presents a plan view of propagation loss, while the right side displays a three-dimensional acoustic field volume rendering and slicing. Figure 7 illustrates a profile view of propagation loss.

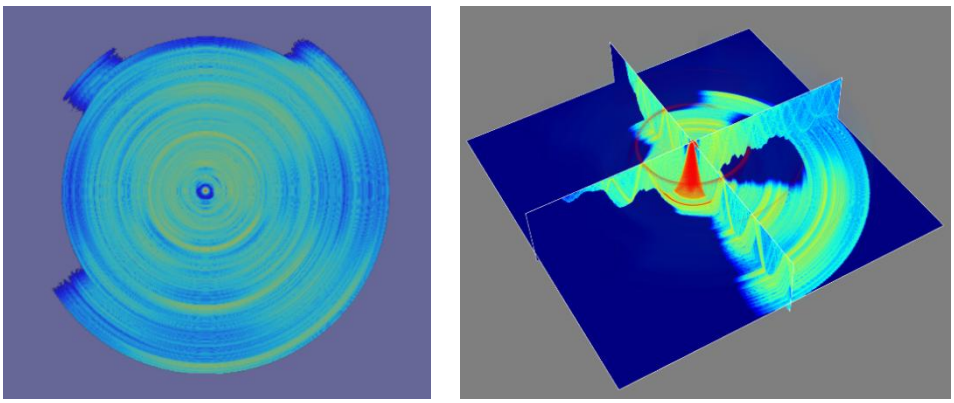

Figure 6 Plan View of Propagation Loss and 3D Acoustic Field Volume Rendering with Slicing

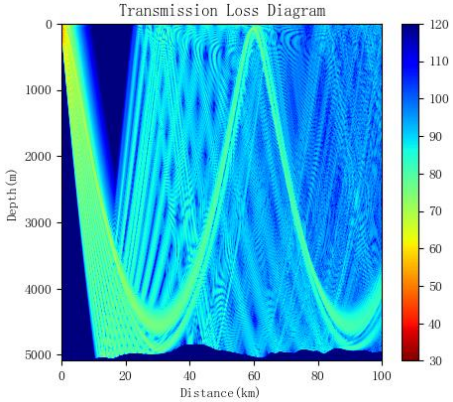

Figure 7 Profile View of Propagation Loss

5 CONCLUSION

Based on the Mayavi scientific visualization engine, this study has developed a marine acoustics simulation visualization platform. By integrating the Bellhop ray-tracing model and the RAM parabolic equation model, and incorporating multi-threaded parallel computing technology, the platform significantly enhances acoustic field simulation efficiency. It effectively addresses the low-efficiency issues associated with traditional single-threaded computational models, enabling real-time dynamic rendering of multi-azimuth acoustic field data.

The platform employs a GIS map and multi-source data fusion architecture, strengthening its capability to represent the spatiotemporal characteristics of marine acoustic data. It supports multi-dimensional coupled analysis of marine environmental data—such as terrain, seabed sediment properties, and sound speed profiles—with acoustic field propagation characteristics. Through interactive 2D/3D visualization techniques, it intuitively reveals the distribution patterns of acoustic fields in complex marine environments. Its modular design supports the extensibility of acoustic models and the dynamic integration of heterogeneous data, laying a flexible foundation for future technological iterations. This provides an efficient tool for underwater acoustic modeling optimization and scientific research decision-making.

Future research will focus on the refined modeling of complex seabed terrain coupling and further enhance the ability to fuse and visualize multi-source heterogeneous data, thereby offering more powerful visual decision support for marine resource exploration.

COMPETING INTERESTS

The authors have no relevant financial or non-financial interests to disclose.

REFERENCES

[1] Kaddouri S, Beaujean PPJ, Bouvet PJ, et al. Least Square and Trended Doppler Estimation in Fading Channel for High-Frequency Underwater Acoustic Communications. IEEE Journal of Oceanic Engineering, 2014, 39(1): 179-188.

[2] Dong L, Dong HF. Bellhop - a modeling approach to sound propagation in the ocean, 2014.

[3] Küsel ET, Siderius M. Comparison of propagation models for the characterization of sound pressure fields. IEEE Journal of Oceanic Engineering, 2019, 44(3): 598-610.

[4] Lu J, Rincon N, Wood DE, et al. Metagenome analysis using the Kraken software suite. Nature Protocols, 2022, 17: 2815-2839.

[5] Yang J, He L, Shuai C, et al. Underwater Acoustic Simulation of Different Seamount Topographies Based on the Bellhop Model. Proceedings of the 11th Youth Academic Conference of the Acoustical Society of China. Beijing: Acoustical Society of China, Youth Working Committee of the Acoustical Society of China, 2015: 4-8.
[6] Chen X, An L. Simulation Method for Underwater Acoustic Channel Impulse Response Based on the RAM Model. Proceedings of the 2018 National Acoustics Conference. Beijing: Acoustical Society of China, 2018: 2.
[7] Li M, Zhou R. Research on Underwater Channel Simulation Method Based on the BELLHOP Model. Ship Electronic Engineering, 2018, 38(8): 166-169.
[8] Wang S. Design and Implementation of an Underwater Sound Field Simulation System Based on the Bellhop Model. Wuhan: Huazhong University of Science and Technology, 2020.
[9] Li Z, Luo X, Zhou Y, et al. A Six-Element Underwater Acoustic Positioning Simulation System Based on Matlab/Simulink. Journal of Hubei University (Natural Science Edition), 2023, 45(4): 581-587.
[10] Ljung M, Hadwiger M, Knapp J, et al. Advanced illumination techniques for GPU volume raycasting. ACM SIGGRAPH Asia Courses. New York: ACM, 2015: 1-166.
[11] Tian L. Research on Visualization of the Footprint Table Method Based on CUDA. Nanjing University of Science and Technology, 2025.
[12] Lacroute P, Levoy M. Fast volume rendering using a shear-warp factorization of the viewing transformation. Proceedings of the 21st Annual Conference on Computer Graphics and Interactive Techniques. New York: ACM, 1994: 451-458.
[13] Ji J. Design and Implementation of a 3D Data Field Visualization System Based on Volume Rendering. China University of Petroleum (East China), 2015.
[14] Yan L. Acoustic Field Characteristics and Software Implementation in Three-Dimensional Complex Sea Areas. Harbin Engineering University, 2022.
[15] Li T, Jiao X, Liu X, et al. Thread-Level Parallelism and Optimization of a 3D Graphics Rendering Engine. National Annual Conference on High Performance Computing. China Computer Federation, China Software Industry Association, 2012.
[16] Huan T. Research on Visualization Techniques for Three-Dimensional Underwater Acoustic Data. Hangzhou Dianzi University, 2017.

Journal of Computer Science and Electrical Engineering
Print ISSN: 2663-1938
Online ISSN: 2663-1946
DOI: https://doi.org/10.61784/jcsee3109

DISTRIBUTION NETWORK OPTIMIZATION STRATEGY AND RELIABILITY ANALYSIS CONSIDERING LARGE-CAPACITY ENERGY STORAGE SYSTEM

WenXiang Liao
Fuzhou Transportation New Energy Technology Co., Ltd, Fuzhou 350002, Fujian, China.

Abstract: As an important distributed power source, energy storage systems are gradually being used in distribution networks. This article is based on the 10kV distribution network system taking into account the large-capacity energy storage system, which introduce the principle of the energy storage system access to the distribution network and analyze the control strategy of the energy storage system under different working modes and propose an optimization modeling method for energy storage system based on genetic algorithm. Finally, using the failure mode consequence analysis method to calculate the reliability analysis index of the distribution system, and then verifing that the application of the energy storage system can improve power supply reliability of distribution network.
Keywords: Energy storage system; Distribution network; Optimization strategy; Reliability analysis; Genetic algorithm

1 INTRODUCTION

The research and development of energy storage technologies have been highly concerned by the energy, transportation, power, and telecommunications sectors in various countries, and have been of great significance to the development of new energy industries. In a sense, the degree of application of energy storage technology will determine the level of new energy development. In the field of electricity, energy storage technology is gradually being applied to distribution networks. When distribution networks are connected to large-capacity energy storage systems, the operation and management of distribution networks will become more complicated[1-3]. Therefore, the analysis of the working mechanism and reliability of energy storage system linked distribution network is a subject worthy of study[4-6]. The connection between energy storage system and distribution network involves four typical operating modes. During the process of switching the operating mode, it is necessary to carry out transition control of the process to avoid large voltage or current impact due to voltage amplitude, frequency, phase and other factors causing the negative impact on the load. The link between energy storage system and distribution network also needs to consider how to optimize the charging and discharging strategy of the scheduling energy storage system to improve the stability of the voltage at the end node of the distribution network[7-10].
Section 1 of this paper describes the working principle of the energy storage system accessing the distribution network, analyzes the grid connection mode of the energy storage system through the PQ control strategy and the off-grid model of the V/F control strategy.Then,designing the system wiring diagram after the energy storage system is connected to the 10kV distribution network to furtherly analyze the process of switching the energy storage system off-grid to off-grid and off-grid switching to the grid. In Section 2 of this paper, based on the genetic algorithm, taking the minimum variance of the load curve as its objective function, and finding the optimal solution within the linear constraints of capacity and charge-discharge power as the optimal scheduling strategy of charge and discharge of the energy storage system for improving the stability of the voltage at the end node of distribution networks that access large-capacity energy storage systems. In section 3 of this paper, the failure mode consequence analysis method is used to calculate the failure rate before and after the energy storage system is connected to the distribution network, the time of blackout of each fault, the annual outage time and the reliability analysis index of the distribution system. The results show that the energy storage system can improve the power supply reliability of the distribution network.

2 ENERGY STORAGE SYSTEM ACCESS PRINCIPLE AND WORKING MODE CONTROL STRATEGY

1.1 Energy Storage System Access Principle

The energy storage system is a system that connects an energy conversion device with an energy storage battery pack and is connected with a power grid to store the grid energy in a battery pack or feed the battery pack energy back to the grid. The schematic diagram of the main working module of energy storage system is shown in Figure 1.
Energy conversion system (PCS) consists of DC/AC three-phase high-frequency bidirectional converter, DC/DC bidirectional buck-boost chopper, PCS control unit. The energy conversion device PCS controller receives the background control instruction through communication, and controls the converter to charge or discharge the battery according to the sign and size of the power instruction to realize the adjustment of the active power and reactive power of the power grid. The PCS controller communicates with the battery management system through the CAN interface and obtains battery pack status information, which can realize protective charge and discharge of the battery and ensure battery operation safety[11].

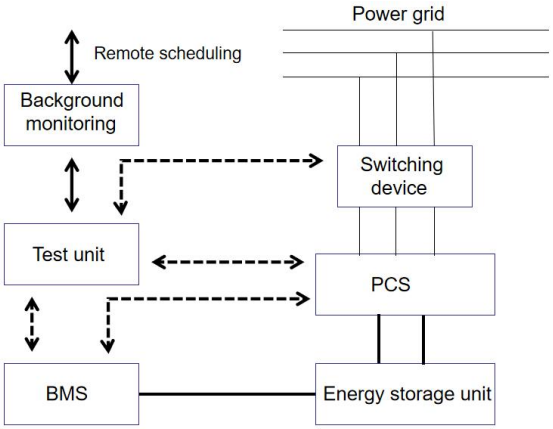

Figure 1 Schematic Diagram of Main Working Modules of Energy Storage System

1.2 Energy Storage System Working Mode Control Strategy

In grid-connected mode, according to the active and reactive power commands, PCS implements active and reactive power control through PQ control strategy. The fundamental sine variable in the stationary three-phase coordinate system is transformed into the direct current component in the synchronous rotating coordinate system through coordinate transformation to realize the decoupling control of active and reactive power in energy-storage grid-connected. When the voltage of the grid is lower than the normal voltage range, the terminal voltage of the grid system is increased by increasing the power output of the energy storage system; conversely, when the voltage is higher than the normal voltage range, the terminal voltage of the power supply system is reduced by the increase of the power absorption of the energy storage system[12-13].

Taking the 1MW/2MWh storage system grid connection as an example, the main wiring diagram of the energy storage system interconnection mode is shown in Figure 2. Both battery packs have a capacity of 1 MWh. After PCS, the DC power is reversed to AC power, then boosted to 10 kV by a step-up transformer, and finally integrated into the grid.

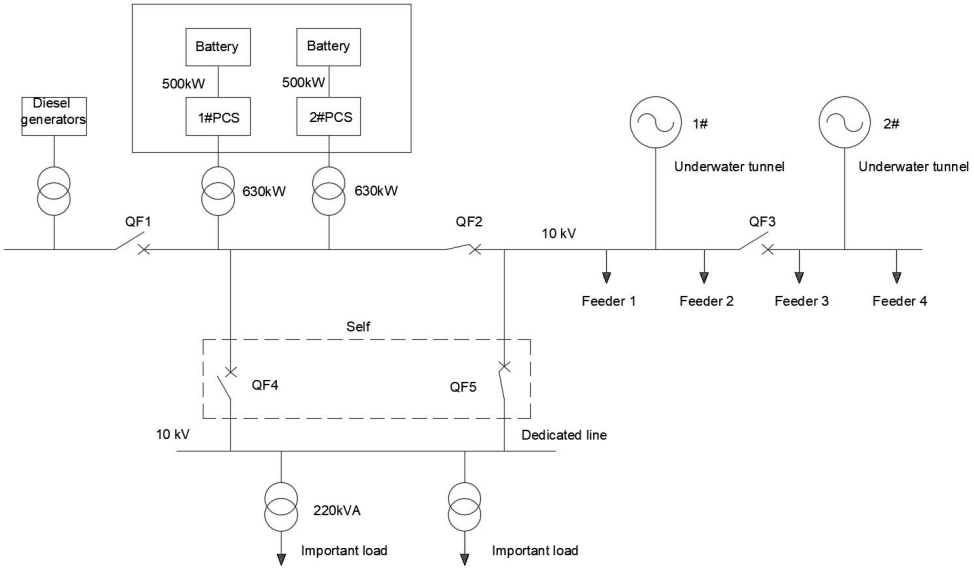

Figure 2 Main Wiring Diagram of the Energy Storage System In Grid Mode

Grid-connected working process: when the two-way power supply is normal, the QF2 and QF5 switches are closed, and the QF3 and QF4 are disconnected. The centralized monitoring system of the energy storage system controls the charge and discharge power of the energy storage system through communication instructions. The energy storage system can be charged during the low-power period. Discharge at the peak of electricity usage and provide reactive power support for distribution network to improve the power quality of the terminal distribution network. When there is a fault in one line of the cable, the energy storage system and the other cable support the load together and do not need to cut the load, which greatly improves the reliability of the power supply of the load.

In the off-grid mode, when the energy storage system operates as the main power source in the power grid or the energy storage system independently supplies power to the load, it must provide voltage (V) and frequency (F) support for the load to maintain the stability of the grid voltage and frequency(V/F control). The centralized controller provides a standard voltage phase reference signal for the PCS, which can output the same voltage phase and frequency when several PCSs are connected in parallel. At the same time, according to the collected total load current and each PCS

current signal, the amplitude of each PCS output voltage is adjusted, and the current sharing control of each PCS can be realized[14].

Figure 3 shows the main wiring diagram of the 1MW/2MWh energy storage system off-grid mode under the V/F control strategy. Monitor the voltage of each node of the system. When the voltage exceeds the limit, adjust the voltage, or adjust the reactive power compensation device nearby, or adjust the energy storage output of the energy storage to restore the system voltage.

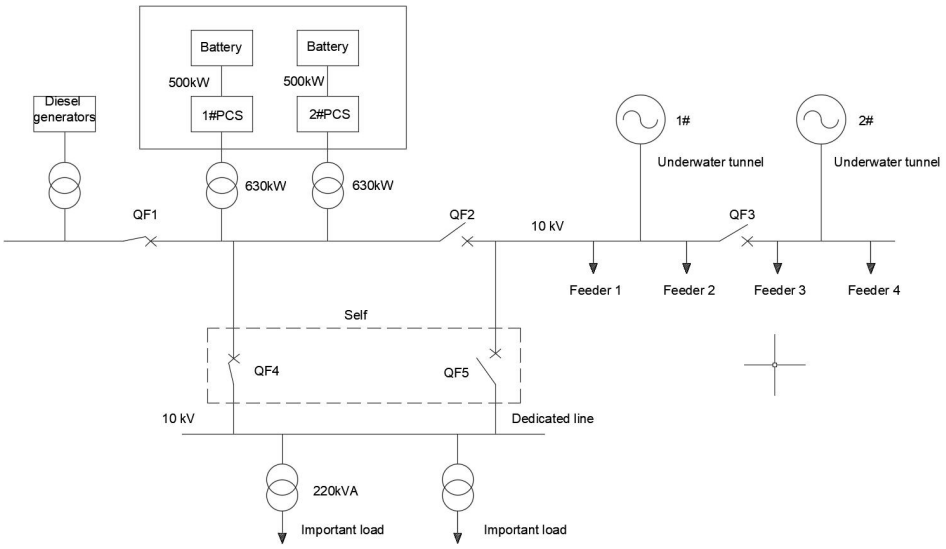

Figure 3 Main Wiring Diagram of the Off-Grid Mode of the Energy Storage System

Off-grid mode working process: When the two cables enter the line fault occurs, the distribution network loses the main power. The centralized monitoring system first controls the QF2 and QF5 switches to open, and issues a command to close the QF4 switch. At the same time, the energy storage system is started in V/F mode through communication instructions. At this time, the energy storage system becomes an off-network working mode, providing power support for important users.

During the main power supply of the PCS, the main power source should be converted to a diesel generator before the PCS discharges to the minimum limit allowed by the remaining capacity (SOC) as the power consumption of the important users increases. The centralized monitoring system of the energy storage system monitors the SOC of the two energy storage battery packs in real time. When the SOC approaches the lower limit value, the QF1 switch is closed, and the diesel generator can charge the energy storage system. This will ensure the reliability of power supply for important loads to the utmost extent.

When the energy storage system is connected to the network, if there is an external fault in the system and the power grid cannot be used as the main power source to provide power to the user, the energy storage system will be converted into the off-network mode and continue to supply power to the important load. This process is called on-grid to off-gird mode.

When the energy storage system is running off-grid, if the external power grid has been repaired and can be used as the main power supply to provide power support for the load, the energy storage system will be changed from the off-grid mode to the grid-connected mode. This process is called off-grid to on-gird mode[15].

Figure 4 shows a schematic diagram of two mode conversion.

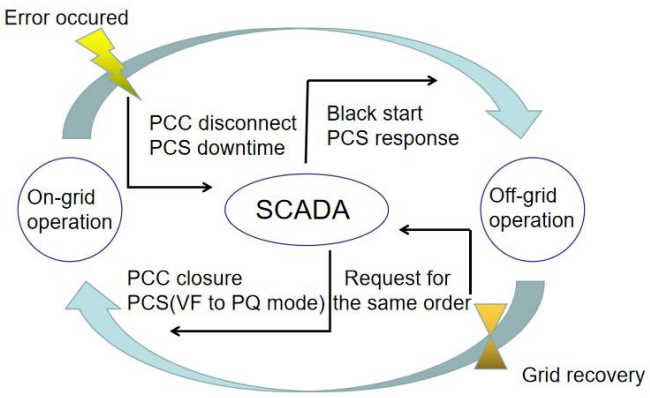

Figure 4 A Schematic Diagram of Two Mode Conversion

3 OPTIMIZATION STRATEGY OF ENERGY STORAGE SYSTEM BASED ON GENETIC ALGORITHM

2.1 Establish an Energy Storage System Optimization Model

The goal of the distribution network is to make the load curve as flat as possible. If the original load of the grid and the output power of the energy storage system are taken as a whole, as the new load of the grid, the goal of the energy storage system modeling is to make the new load curve as flat as possible without large peaks and troughs.
The variance can reflect the extent to which the load curve connected by a series of points deviates from its average. Therefore, the variance of the load curve is selected to establish the optimization model of the energy storage system.
The objective function of the energy storage system optimization model is

$$\min f(\mathrm{P}) = \frac{1}{n}\sum_{i=1}^{n}[F(i)+P(i)-\frac{1}{n}\sum_{i=1}^{n}(F(i)+P(i))]^{2} \tag{1}$$

Among them, $F(i)+P(i)$ Is the new load value of the grid, $\sum_{i=1}^{n}(F(i)+P(i))$ is the load average ，n represents the number of load data in a day, $F(i)$ is the load value at time i, $P(i)$ is the output power of the energy storage system at time i, $P(i)$ is the output power of the energy storage system at time i. When the energy storage system is charged, $P(i)$ is positive. When the energy storage system is discharged, $P(i)$ is negative.
The linear constraints of the energy storage system optimization model include:

① Power constraints of energy storage systems satisfy

$$-P_{\max} \le P(i) \le P_{\max}, i = 1,2,\cdots n \tag{2}$$

② Capacity constraints of energy storage systems satisfy

$$S_{\min} < S(i) < S_{\max}, i = 1,2,\cdots n \tag{3}$$

2.2 An Algorithm for Solving Energy Storage System Optimization Model Based on Genetic Algorithm

Set the capacity of the energy storage system to 500kW/1MWh and 1MW/2MWh, and find the optimal solution of the optimal model for the energy storage system under different capacity sizes. Figure 5 shows the hourly load data of the distribution network 24 hours a day.

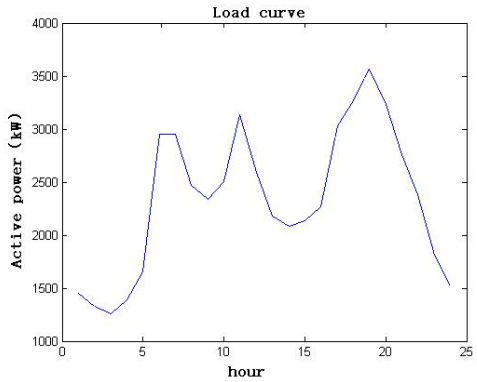

Figure 5 The Hourly Load Data of the Distribution Network 24 Hours a Day

Using genetic algorithm to solve the energy storage system optimization model:

$$\begin{aligned}\min f(P) = (\frac{1}{n}-\frac{1}{n^2})\sum_{i=1}^{n}(P(i))^2 - \frac{1}{n^2}[2p(1)p(2)+2p(1)p(3)+\cdots+2p(n-1)\\ p(n)]+\{[\frac{2}{n}F(1)-\frac{2}{n^2}\sum_{i=1}^{n}(F(i)]p(1)+[\frac{2}{n}F(2)-\frac{2}{n^2}\sum_{i=1}^{n}(F(i)]p(2)\\ +\cdots+[\frac{2}{n}F(n)-\frac{2}{n^2}\sum_{i=1}^{n}(F(i)]p(n)\}+4.4728\times 10^5\end{aligned} \tag{4}$$

Where, 4.4728×10^5 is the calculated value of the constant term;
the capacity constraint of the energy storage system of the energy storage system is $5\%S \le S(i) \le 95\%S$;
The charge and discharge power constraints of the energy storage system are $-500kW \le P(i) \le 500kW$;
The initial and final charge of the energy storage system are $S_0 = 10\%S$ and $S_1 = 80\%S$ respectively.

2.2.1 Optimization model of energy storage system with capacity of 500kW/1MWh

Set the number of terminations R=100. After 100 iterations, the best fitness curve, average fitness curve and optimal adaptation are shown in Figure 6. The best fitness at this time is best fitness=284690.7948. That is, the minimum value of the energy storage system optimization model is: $\min f(P) = 2.8649 \times 10^5$

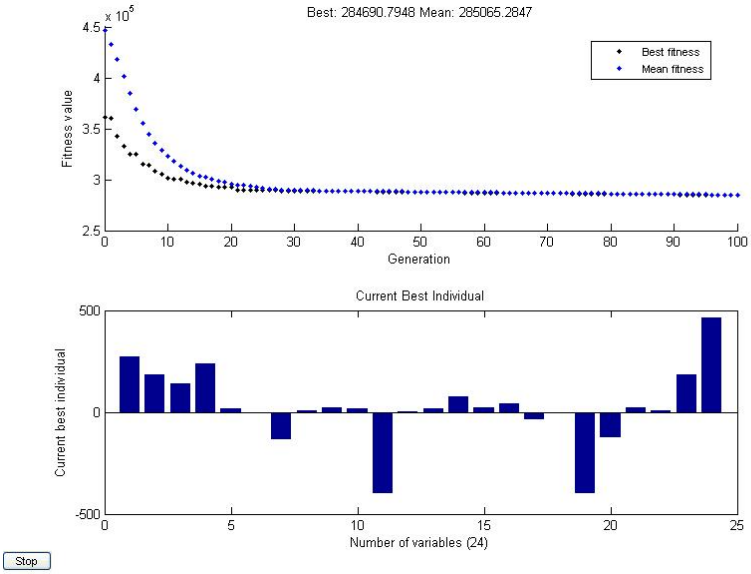

Figure 6 Best Fitness, Average Fitness, Best Individual Curve

After 30 iterations, the optimal fitness curve and the average fitness curve tend to be stable. After 100 iterations, the optimization results are shown in the power curve of the energy storage system in Figure 7.

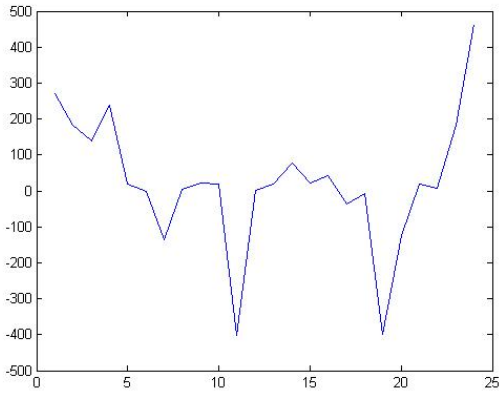

Figure 7 Energy Storage System Power Curve

The comparison of the original load curve and the load curve after the peak-filling of the energy storage system is shown in Figure 8.

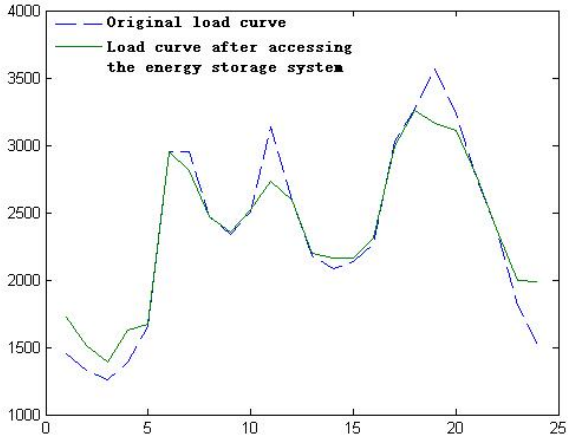

Figure 8 Comparison of Load Comparison Curves before and after Peak Filling

After the charge and discharge of the energy storage system, the maximum load curve max(P)=3260.9 kW, and the minimum value min(P)=1394.6 kW.

2.2.2 Optimization model of energy storage system with capacity of 1MW/2MWh

Set the number of terminations R=100. After 100 iterations, the best fitness curve, average fitness curve and optimal adaptation are shown in Figure 9. The best fitness at this time is best fitness=175300.1481. That is, the minimum value of the energy storage system optimization model is: $\min f(P) = 1.7530 \times 10^5$

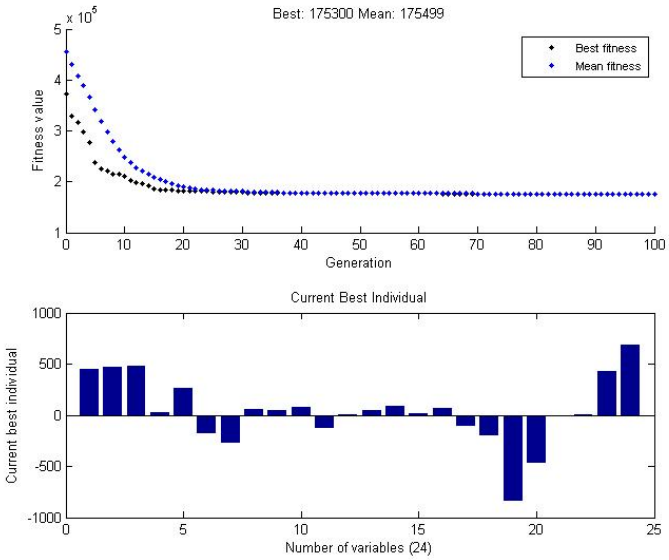

Figure 9 Best Fitness, Average Fitness, Best Individual Curve

After 30 iterations, the fitness curve gradually stabilized. After 100 iterations, the optimization results are shown in Figure 10.

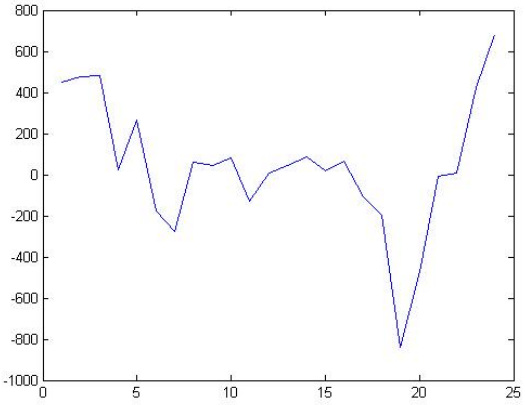

Figure 10 Energy Storage System Power Curve

The comparison of the original load curve and the load curve after the peak-filling of the energy storage system is shown in Figure 11.

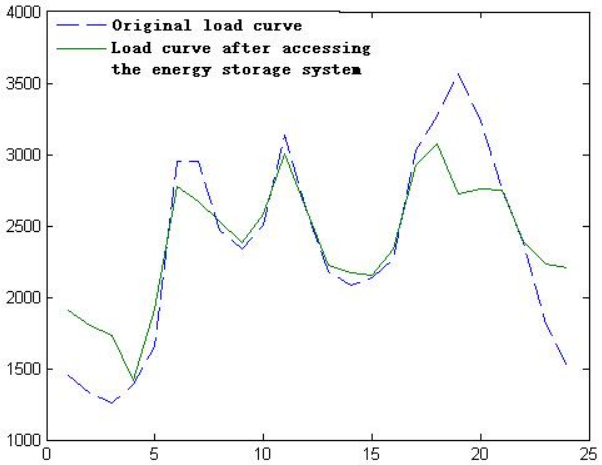

Figure 11 Comparison of Load Comparison Curves before and after Peak Filling

After the charge and discharge of the energy storage system, the maximum load curve max(P)=3071kW, and the minimum value min(P)=1414.9kW.

2.3 Optimization Strategy Effect Analysis

The optimal solution of the energy storage system optimization model based on genetic algorithm plays a role in peak clipping and filling. The optimal fitness value corresponding to the best individual obtained by genetic algorithm has a great relationship with the capacity of the energy storage system. The larger the capacity, the smaller the variance of the load curve and the flatter the load curve.

4 DISTRIBUTION SYSTEM RELIABILITY ANALYSIS

The medium voltage distribution system is mostly a ring network with open loop operation, which can be treated as a radial system. The reliability analysis method adopted is the failure mode consequence analysis method($FMEA$). For a series system, the following formula is used

$$\lambda_s = \sum_{i=1}^{n} \lambda_i \tag{5}$$

$$r_s = \frac{\sum_{i=1}^{n} \lambda_i r_i}{\sum_{i=1}^{n} \lambda_i} = \frac{U_s}{\lambda_s} \tag{6}$$

$$U_s = \sum_{i=1}^{n} \lambda_i r_i = \lambda_s r_s \tag{7}$$

Where， λ_s is the average failure rate of the system load point (time / year), λ_i is component failure rate (time / year), r_i is the component repair time (hours/times), r_s is the equivalent repair time (hours/times) for each faulty system load point, U_s is the system unavailability rate, that is, the annual power outage time of the load point (hour/year).

For parallel systems, the following formula is used

$$\lambda_p = \lambda_1 \lambda_2 (r_1 + r_2) \tag{8}$$

$$r_p = \frac{r_1 r_2}{r_1 + r_2} \tag{9}$$

$$U_p = \lambda_p r_p = \lambda_1 \lambda_2 r_1 r_2 \tag{10}$$

when two components are connected in parallel

$$\lambda_p = \lambda_1 \lambda_2 \lambda_3 (r_1 r_2 + r_1 r_3 + r_2 r_3) \tag{11}$$

$$r_p = \frac{r_1 r_2 r_3}{r_1 r_2 + r_1 r_3 + r_2 r_3} \tag{12}$$

$$U_p = \lambda_p r_p = \lambda_1 \lambda_2 \lambda_3 r_1 r_2 r_3 \tag{13}$$

Where， λ_1、λ_2、λ_3 are the failure rate of components 1, 2, 3 (time / year), r_1、r_2、r_3 a, b, c are the fault repair time of components 1, 2, 3 (hours / times), λ_p is the average failure rate of the system load point (times / year), r_p is the equivalent repair time for each faulty system load point, U_{p} is the system unavailability rate, that is, the annual power outage time (hour/year) of the load point.

Distribution system reliability analysis indicators related to users:

System average interruption frequency index($SAIFI$)

$$SAIFI = \frac{\text{Total number of user power outages}}{\text{Total number of users}} = \frac{\sum \lambda_i N_i}{\sum N_i} \tag{14}$$

Where， the unit of $SAIFI$ is: times / (user · year), λ_i is the failure rate， N_{i} is the number of users of load point i.

Customer average interruption frequency index($CAIFI$)

$$CAIFI = \frac{\text{Total number of user power outages}}{\text{Total number of users affected by power outages}} \tag{15}$$

Where， the unit of $CAIFI$ is: times / (blackout user · year).。

System average interruption duration index($SAIDI$)

$$SAIDI = \frac{\text{Total user power outage time}}{\text{Total number of users}} = \frac{\sum U_i N_i}{\sum N_i} \tag{16}$$

Where, the unit of $SAIDI$ is: h/(user· year)， U_{i} is the annual power outage time， N_i is the number of users of load point i.

Customer average interruption duration index($CAIDI$)

$$CAIDI = \frac{\text{Total user power outage time}}{\text{Total number of user power outages}} = \frac{\sum U_i N_i}{\sum \lambda_i N_i} \tag{17}$$

Where, the unit of $CAIDI$ is: h/(blackout user·year)， λ_i is the failure rate， U_{i} is the annual power outage time， N_i is the number of users of load i.

Average serviceav ailability index($ASAI$)

$$ASAI = \frac{\text{Total user power supply hours}}{\text{Total number of hours the user requests power}} = \frac{\sum N_i \times 8760 - \sum U_i N_i}{\sum N_i \times 8760} \tag{18}$$

In the formula， 8760 is the number of hours in a year.

Average service unavailability index($ASUI$)

$$ASUI=1-ASAI=\frac{\sum U_i N_i}{\sum N_i \times 8760} \tag{19}$$

3.1 Reliability Calculation

Assume that the circuit breaker bus and power supply mains breakers in the distribution network system are completely reliable. When a certain part of the system fails, just disconnect the isolation switch of its branch to disconnect the fault area and restore the system.

(1)Reliability calculation of distribution network system before energy storage system is connected,as shown in Figure 12.

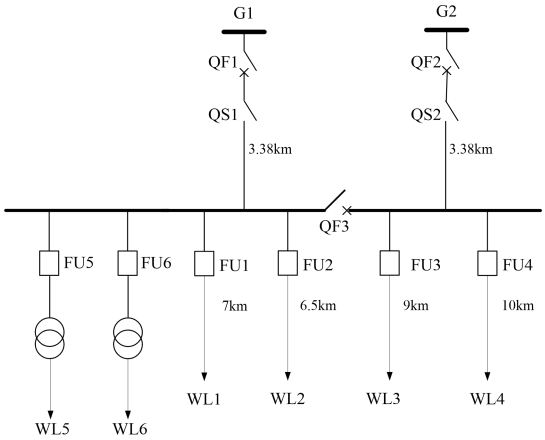

Figure 12 Wiring Diagram of the Distribution System before the Energy Storage System is Connected

Through the failure mode consequence analysis method, the reliability analysis index of the distribution network system before the energy storage system is accessed can be obtained, as shown in Table 1:

Table 1 Reliability Analysis Indicators of the Distribution Network System before the Energy Storage System is Connected

Reliability index	SAIFI	CAIFI	SAIDI	CAIDI	ASAI	ASUI	ACCI
Unit	Time/(user·year)	Times / (blackout users · years)	h/(user·year)	h/(blackout user·year)			kWh
value	1.489	1.489	9.8316	6.6026	0.998878	0.001122	3.9049

(2) Reliability calculation of distribution network system after energy storage system is connected,as shown in Figure 13.

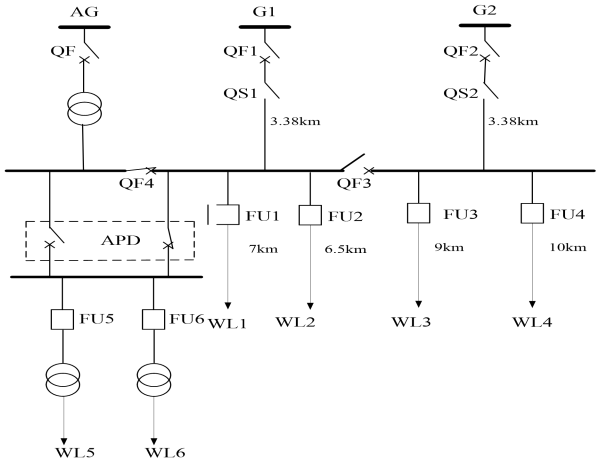

Figure 13 Wiring Diagram of the Distribution System after the Energy Storage System is Connected

Through the failure mode consequence analysis method, the reliability analysis index of the distribution network system after the energy storage system is connected can be obtained, as shown in Table 2 and Table 3:

Table 2 Reliability Analysis Indicators of Distribution Network System after Energy Storage System Access

Reliability index	SAIFI	CAIFI	SAIDI	CAIDI	ASAI	ASUI	ACCI
Unit	Time/(user·year)	Times / (blackout users · years)	h/(user·year)	h/(blackout user·year)			kWh
value	1.467	1.467	9.5012	6.4734	0.998915	0.001085	3.7618

Table 3 Critical Load Reliability Analysis Table

index	failure rate(λ)	Power failure time each time(r)	Annual blackout time(u)
Original system	0.2707	3.4034	0.9213
After the energy storage system is connected	0.2531	2.5942	0.6566

3.2 Reliability Conclusion Analysis

After the energy storage system is connected to the power distribution system, the failure rate of the important load, the average time per failure, and the annual power outage time on the two feeders of WL5 and WL6 are significantly reduced. The failure rate of important loads decreased from 0.2707 to 0.2531, and the average time per failure was reduced from 3.4034 hours to 2.5942 hours. The annual average power outage time was reduced from 0.9213 hours to 0.6566 hours. The energy storage system has an obvious effect on improving the reliability of power supply for important loads.

Calculate the reliability index based on all the load of the power distribution system, and compare the data before and after the energy storage system is connected to the power distribution system. The results show that the total number of power outages of users decreased from 17198.35 times to 16952.23 times, and the total duration of power outages decreased from 113,554.67 to 109,739.37. The average number of power outages decreased from 1.489 to 1.467 and the average user power outage duration was reduced from 6.6026 to 6.4734 times. The number of power outages and power outages were significantly reduced.

Finally, compare them with the average power availability indicator. Before the energy storage system is connected, the average power supply availability of the power distribution system is 0.998878. After the energy storage system is connected, the average power supply availability of the power distribution system is 0.998915, and the reliability is effectively improved.

5 CONCLUSION

Insufficient power supply capacity at the end of the distribution network has always been a major concern in power grid operation. As an important distributed power source, energy storage system plays an active role in power grid peak-filling, new energy access, power quality improvement and emergency power supply. Based on the 10kV distribution network system considering large-capacity energy storage system, this paper proposed the optimal control strategy for charge and discharge of energy storage system based on analyzing the principle that the energy storage system is connected to the distribution network and the control strategy of the energy storage system under different working modes and genetic algorithm. It is concluded that the larger the capacity of the stored energy storage system, the smaller the variance of the load curve and the flatter the load curve. Finally, the failure mode consequence analysis method is used to calculate the reliability analysis index of the distribution system. The calculation results show that after the energy storage system is connected, the failure rate of the load, the average time of each failure, and the annual power outage time are significantly reduced, and the average power supply availability rate is improved. It is verified that the application of the energy storage system can improve the reliability of the power supply of the distribution network.

COMPETING INTERESTS

The authors have no relevant financial or non-financial interests to disclose.

REFERENCES

[1] Evangelopoulos V A, Georgilakis P S. Optimal distributed generation placement under uncertainties based on point estimate method embedded genetic algorithm. Transmission & Distribution, 2014, 8(3): 389-400.

[2] Wei W, Pan Z C, Cong W, et al. Impact of Distributed Generation on relay protection and its improved measures. IEEE Electricity Distribution, 2008: 1-5.

[3] Cui J, Yang J Y, Li L F, et al. Voltage fluctuation analysis and mitigation of distribution network containing distributed wind farm. Power System Technology, 2015, 39(12): 3414-3420.

[4] Hao S, Chiang H D. CDFLOV: A practical tool for tracing stationary behaviors of general distribution networks. IEEE Transactions on Power Systems, 2014, 25(3): 1365-137.
[5] Zhang L M, Tang W, Zhao Y J, et al. Analysis of the effect on the system voltage and loss of distributed generation connected to distribution network. Power System Protection and Control, 2011, 39(5): 91-97.
[6] Wu X M, Liu J, Bi P X. Research on voltage stability of distribution networks. Power System Technology, 2006: 31-35.
[7] Li B W, Li P J, Wei H. A nonlinear programming model for improving type switching logic of PV-PQ nodes in power flow calculation. Power System Technology, 2009: 32-43.
[8] Michael E, Ramesh R. The impact of single-phase grid-connected distributed photovoltaic systems on the distribution network using P-Q and P-V models. International Journal of Electrical Power and Energy Systems, 2017, 91: 20-33.
[9] Luo Y L, Li Y, Wu K. Dynamic global optimal power flow and its two-stage control algorithm of a power grid integrated with wind power farms. Electrical Power, 2013: 131-137.
[10] Chen H Y, Chen J F, Shi D Y, et al. Power flow study and voltage stability analysis for distribution systems with distributed generation. Power Engineering Society General Meeting, 2006.
[11] Zhou J A, Su H S. Back/forward sweep power flow calculation with distributed generation considering static load characteristics. Power System Protection and Control, 2015: 26-32.
[12] Mao W J, Li H W, Li C. A distribution system reconfiguration method considering the optimal active power dispatching of DGs. Power System Protection and Control, 2017: 57-63.
[13] Li T Y, Han Y Q, Hu X Q, et al. Characteristics of static voltage stability for distributed generation integrated into power system and its impacts analysis. Power System Protection and Control, 2014: 8-13.
[14] Ma R, Zhou Z F, Xu H M, et al. Dynamic voltage collapse index with wind speed considering. Journal of Electric Power Science and Technology, 2009: 41-46.
[15] Wang X T, Shi L, Ren J W, et al. Optimized configuration of distributed generators based on power circle. Electric Power Science and Engineering, 2012: 28-32.

Journal of Computer Science and Electrical Engineering
Print ISSN: 2663-1938
Online ISSN: 2663-1946
DOI: https://doi.org/10.61784/jcsee3110

SMOKE DECOY DEPLOYMENT STRATEGIES BASED ON HYBRID INTELLIGENT OPTIMIZATION MODELS

TianJian Zhong
School of Automation, Central South University, Changsha 410083, Hunan, China.

Abstract: This paper systematically investigates optimal deployment strategies for smoke decoys launched by unmanned aerial vehicles (UAVs) to defend against high-speed incoming missiles in complex dynamic scenarios. The research is of significant importance for enhancing the survivability of high-value assets by providing a theoretical foundation and practical optimization tools for intelligent and adaptive smoke countermeasure systems. The research spans from high-precision calculation of effective duration to continuous multi-decoys shielding by a single UAV. First, for calculating effective shielding duration under fixed parameters, a three-dimensional kinematic model was established to characterize the spatial relationships among the missile, the drone's parabolic motion, and the uniform descent of the smoke cloud. Using three-dimensional geometric shielding criteria and a high-resolution time-stepping method, the effective shielding duration achieved by the FY1 drone deploying a single decoy against the M1 missile was precisely calculated to be approximately 1.412 seconds. Subsequently, the problem was elevated to single-deployable parameter optimization. A nonlinear constrained optimization model was constructed with the objective of maximizing masking duration, incorporating decision variables such as the UAV's heading angle, flight speed, deployment timing, and detonation delay. To address the non-differentiable nature of this objective function, a hybrid genetic algorithm and particle swarm optimization method was employed for global search and local refinement. This approach ultimately maximized effective masking duration to 4.690 seconds, with analysis indicating deployment timing and detonation delay as the most critical parameters. Finally, for a single-UAV multi-munition continuous shielding strategy, this paper designed a two-stage analytical-numerical hybrid model: "inverse solution for optimal detonation points followed by forward inversion of UAV strategy." Through the synergistic evolution of the particle swarm optimization framework and GA-PSO, the deployment interval constraints between multiple decoys were successfully resolved, achieving seamless relay between two decoys. The total effective masking duration reached 9.020 s, demonstrating that the proposed model can obtain high-quality solutions with both accuracy and robustness under complex constraints.
Keywords: Smoke decoy deployment strategy; Genetic algorithm; Particle swarm optimization

1 INTRODUCTION

With the widespread deployment of precision-guided weapons on modern battlefields, enhancing the survivability of critical assets has become a paramount challenge. Smoke countermeasures, as a low-cost, flexible passive defense method, have gained prominence for their ability to effectively obscure optical and infrared detection. In recent years, the precise deployment of smoke countermeasure munitions via unmanned aerial vehicle (UAV) platforms has emerged as a tactical approach[1-2]. UAVs offer advantages such as rapid response and reusability, significantly enhancing coverage effectiveness and countermeasure persistence. However, achieving efficient smoke interference requires solving a core technical challenge: due to the high speed of incoming missiles and the limited duration of smoke screens, precise planning of the drone's flight path, deployment timing, and detonation location is essential to maximize effective concealment time for the true target. Previous studies addressing dynamic target concealment often simplified geometric criteria or time steps, resulting in insufficient prediction accuracy and inadequate support for optimization decisions in complex multi-deployment scenarios[3]. This research aims to establish a high-precision model for accurately calculating the effective concealment duration of smoke against dynamic targets, and to design optimized deployment strategies from single-deployment to multi-deployment scenarios per drone. The primary innovations in this section are: First, a three-dimensional kinematic model encompassing the trajectories of missiles, UAVs, and smoke grenades was constructed. High-precision concealment duration calculations were achieved using geometric criteria such as “line segment–sphere intersection.” Second, for the single-deployment optimization problem, a two-stage hybrid intelligent optimization framework combining GA and PSO was introduced, effectively addressing complex constrained optimization issues involving non-differentiable objective functions. Finally, for multi-munition coordination, we developed an analytical-numerical hybrid optimization model featuring “reverse-solving optimal layouts followed by forward strategy inversion”. Leveraging the GA-PSO co-evolution mechanism, this model resolves minimum separation constraints for multi-munition deployment, achieving continuous spatio-temporal coverage. This research will follow a progressive approach: fixed-parameter calculation → single-munition parameter optimization → multi-munition sequence optimization[4-5].

2 SINGLE-MISSILE FIXED-PARAMETER SHIELDING VERIFICATION MODEL

2.1 Model Establishment

2.1.1 Missile motion model

In a 3D Cartesian coordinate system (with the decoy target as the origin and the real target located at (0, 200, 0)), missile M1 flies straight towards the decoy target at a constant speed. UAV FY1 flies at a constant altitude and speed, releases the jamming bomb at a predetermined launch time. The jamming bomb undergoes a "horizontal constant velocity + vertical free fall" motion to reach the detonation point, then forms a spherical smoke cloud with a radius r_c=10 m that sinks uniformly at v_s=3 m/s for a duration of T_c=20 s. Obscuration is essentially a geometric judgment problem where "the minimum distance from the smoke cloud center to the missile-real target line of sight does not exceed r_c and the smoke cloud is located between them". For robustness, two additional criteria—"line segment-sphere intersection" and "missile inside the cloud"—are supplemented to avoid missing traversal scenarios due to discrete step sizes [6].

$$x_M(t)=p_{M0}+v_M u_M t,\ u_M=\frac{o_F-p_{M0}}{\|o_F-p_{M0}\|},\ v_M=300\ \text{m/s} \tag{1}$$

where p_{M0} is the initial position of the missile at t=0 (20000, 0, 2000).

2.1.2 UAV model

UAV FY1 flies towards the decoy target at a speed v_F=120 m/s with an initial position (17800, 0, 1800) and a launch time $t_{1,1,p}$=1.5 s. Its launch point is:

$$p_{i,j}(t_{1,1,p})=f_1+v_1 \cdot u_F t_{1,1,p} \tag{2}$$

2.1.3 Smoke bomb model

After launch, the smoke bomb is only affected by gravity and performs a projectile motion, detonating after a delay of σ=3.6 s. Its detonation point is:

$$b_{1,1}=p_{i,j}(t_{1,1,p})+v_1 \cdot u_F\sigma-\frac{1}{2}g\sigma^2 e_z \tag{3}$$

where e_z=(0,0,1).

2.1.4 Smoke cloud model

A spherical cloud is formed instantaneously upon detonation with a constant radius r_c=10 m, and the center sinks uniformly at v_s=3 m/s:

$$c(t)=\left(b_{1,1,x},b_{1,1,y},b_{1,1,z}-v_s t\right),\ 0\le t\le 20 \tag{4}$$

2.1.5 Obscuration judgment conditions

To determine if the missile is obscured by smoke in the direction of the real target, the following conditions must be satisfied simultaneously:

Distance Condition: The perpendicular distance from the smoke center to the "missile-real target" line of sight ≤ r_c;

Orientation Condition: The smoke is located between the missile and the real target, i.e., $(c(t)-x_M(t)) \cdot (x_T-x_M(t))>0$.

When the above conditions are met within the effective period, the missile's line of sight is obscured. The total obscuration duration is the length of the union of these time intervals.

2.2 Solution

This paper implemented numerical simulation using Python (NumPy+Matplotlib) and adopted the time-stepping method (Δt=0.001 s) to judge the obscuration conditions point by point.

Algorithm Steps:

Initialize parameters (initial positions and velocities of the missile/UAV, launch and detonation times, smoke parameters);

Calculate the UAV's launch point and the smoke bomb's detonation point coordinates;

Define the trajectory functions of the missile and smoke: $x_M(t)$ and c(t);

Iterate within the effective time window of the cloud: judge the obscuration conditions point by point;

Count the continuous time intervals that meet the conditions and accumulate their total length;

Output the start time, end time, and total duration of obscuration.

Key Results:UAV flight vector: [-120, 0, 0.1];Launch point coordinates: [17620, 0, 1800]; Detonation point coordinates: [17188, 0, 1736.496]; Initial missile velocity vector: [-298.51115706, 0, -29.85111571]; Missile flight duration: 67.00s; Effective obscuration time: 1.412 seconds;Obscuration start time: 8.038 seconds; Obscuration end time: 9.449 seconds

2.3 Result Analysis

The missile approaches at high speed from 20000 m away and passes through the cloud area within approximately 8–9.5 s, resulting in a brief obscuration. The obscuration time is about 1.4 s, which is significantly lower than the maximum effective duration of 20 s for the smoke, indicating that a single fixed launch is difficult to provide long-term protection.

Longitudinal comparison shows that the missile approaches rapidly at a descending speed of about 30 m/s, while the cloud only sinks at 3 m/s. Their height curves intersect briefly around ≈8 s. Combined with the horizontal distance constraint, the obscuration window can only occur during this period, after which the missile quickly escapes the cloud's influence.

3 SINGLE-MISSILE PARAMETER OPTIMIZATION AND INTELLIGENT ALGORITHM SOLUTION

3.1 Model Establishment

UAV FY1 launches one smoke jamming bomb and needs to independently select its flight direction angle θ_1, flight speed v_1, launch time $t_{1,1,p}$, and detonation delay $t_{1,1,b}$ to maximize the effective obscuration time for missile M1. This is essentially a constrained optimization problem that elevates Problem 1 from a single calculation task to a complex optimization scenario. Under the coupled conditions of UAV kinematics and smoke dynamics, a nonlinear optimization model targeting effective obscuration duration is constructed[7-8].

Given the initial position f_0=(17800,0,1800), the UAV's position at time t is:

$$x_F(t)=f_0+v(\cos\theta,\sin\theta,0)\cdot t \tag{5}$$

The UAV launches the jamming bomb at t_d, and the launch point is:

$$p_{1,1}=x_F(t_d) \tag{6}$$

After launch, the smoke bomb moves in the same direction as the UAV and performs a projectile motion:

$$x_{smoke}(t)=p_{1,1}+(v\cos\theta,v\sin\theta,0)(t-t_d)-\frac{1}{2}g(t-t_d)^2e_z \tag{7}$$

At the detonation time $t_b=t_d+\sigma$, the position of the smoke bomb is the detonation point:

$$b_{1,1}=x_{smoke}(t_b) \tag{8}$$

Consistent with Single-Missile Fixed-Parameter Shielding Verification Model.

Consistent with Single-Missile Fixed-Parameter Shielding Verification Model.

Consistent with Single-Missile Fixed-Parameter Shielding Verification Model.

The missile is considered obscured by smoke if and only if the following conditions are met:

Geometric Condition: The perpendicular distance from the smoke center to the "missile-real target" line $\leq r_c$;

Orientation Condition: The smoke is located between the missile and the real target: $(c(t)-x_M(t))\cdot(x_T-x_M(t))>0$;

Time Condition: $t\in[t_b,t_b+T_c]$.

The objective function is to maximize the effective obscuration time, with constraints including:

$$70\leq v\leq 140 \tag{9}$$

$$t_d\geq 0,\ \sigma>0 \tag{10}$$

$$z_b\geq 0,\ \theta\in[0,2\pi] \tag{11}$$

This is a complex nonlinear optimization problem with multiple constraints.

3.2 Solution

Due to the discontinuous and non-differentiable nature of the objective function, traditional analytical methods are difficult to apply. This paper adopts a two-stage intelligent optimization algorithm (GA+PSO):

Stage 1 (Genetic Algorithm, GA): Perform global search through selection, crossover, mutation, and other operations to quickly find the approximate feasible solution region.

Stage 2 (Particle Swarm Optimization, PSO): Conduct local refined search near the solution provided by GA to improve convergence accuracy [9-10].

Algorithm Steps:

Initialization: Set the population size to 30 and the number of evolution generations to 80 (first 40 generations for GA, last 40 generations for PSO).

Genetic Operations: Adopt roulette selection, multi-point crossover (probability 0.85), and Gaussian mutation (probability 0.2).

Particle Swarm Operations: Use an inertia weight ω=0.5 and learning factors c_1=1.8, c_2=1.2.

Objective Function Calculation: Call the obscuration time calculation function calculate_smoke_obscuration and return the effective obscuration duration.

Convergence Criterion: Terminate early if the improvement of the objective function is <0.01 for consecutive iterations.

Key Results:

Before optimization (Problem 1), the effective obscuration time was approximately 1.4 s.

After optimization, the optimal parameter combination is:

Flight direction angle θ=3.0862 rad (≈176.83°)

Flight speed v=70.00 m/s

Launch time t_d=0 s

Detonation delay σ=2.5 s

Maximum effective obscuration time increased to 4.690 s

Two-stage optimization completed!

Maximum effective obscuration time: 4.690s

Optimal parameters:

Direction angle: 3.0862 rad (≈176.83°)

UAV speed: 70.00 m/s

Launch time: 0.00 s

Detonation delay: 2.59 s

UAV speed vector: [-69.89275977, 3.87325862, 0]
Launch point position: [17800, 0, 1800]
Detonation point position: [17625.5580, 9.66707976, 1769.47654]
Missile speed vector: [-298.51115706, 0, -29.85111571]
Initial missile position: [20000, 0, 2000]
Missile arrival time at decoy target: 67.08 s

3.3 Result Analysis

The optimization results show that the UAV needs to launch the jamming bomb earlier and fly at a lower speed to bring the smoke cloud closer to the missile's path; the obscuration window is significantly extended from the original 1.4 s to 4.690 s.
Sensitivity analysis indicates:
Launch time t_d and delay time σ are the most critical variables with the greatest impact on the results;
Flight direction angle θ is the next most important, requiring alignment near the missile's flight path;
The effect of UAV speed v is relatively weak, only needing to be maintained within a reasonable range.
This suggests that optimization should focus on the precise control of time parameters, while speed and angle serve as auxiliary adjustments.

4 COOPERATIVE OPTIMIZATION FOR CONTINUOUS DEPLOYMENT OF MULTIPLE MISSILES FROM A SINGLE PLATFORM

4.1 Model Establishment

This paper needs to use a single UAV FY1 to continuously launch three smoke jamming bombs to implement multi-stage obscuration jamming against the incoming missile M1, with the goal of maximizing the total effective obscuration time. Since different clouds can overlap or connect in time, the key to the problem is to reasonably arrange the launch interval and detonation time so that the missile remains in an obscured state during the critical flight phase. Direct numerical search is computationally expensive; therefore, it is necessary to analyze the spatial distribution of the effective obscuration area of the smoke based on geometric mechanisms, establish an optimal obscuration position model, and use a reverse derivation method to first determine the optimal detonation point, then infer the UAV's flight direction, speed, and launch sequence. In this process, both the launch interval constraint and UAV flight constraint must be considered to ensure that the three smoke bombs form continuous obscuration in time and space.

4.1.1 Spatiotemporal discrimination model for effective obscuration

Assume the position of missile M1 at the time of detection by the early warning radar is:

$$P_{M1}^{(0)}=(20000,0,2000)\ \text{m}, \tag{12}$$

and it flies straight towards the decoy target $O_{fake}=(0,0,0)$ at a constant speed $v_M=300$ m/s. The center of the real target is:

$$O_{real}=(0,200,0)\ \text{m}. \tag{13}$$

At any time t, the missile's position is:

$$P_{M1}(t)=P_{M1}^{(0)}+v_M \cdot t \cdot n_M, \tag{14}$$

where the unit direction vector is:

$$n_M=\frac{O_{fake}-P_{M1}^{(0)}}{\left\|O_{fake}-P_{M1}^{(0)}\right\|}. \tag{15}$$

The i-th smoke bomb instantly generates a spherical cloud with a radius R=10 m at the detonation point $B_i=(x_i,y_i,z_i)$ at time $t_{i,b}$ and sinks uniformly at $v_s=3$ m/s. Then, at time $\tau\geq 0$ after detonation, the cloud center is:

$$S_i(\tau)=B_i-(0,0,v_s\tau). \tag{16}$$

The necessary and sufficient conditions for effective obscuration are:
The cloud is still within the effective duration, i.e., $\tau\in[0,T_c]$, $T_c=20$ s;
The cloud blocks the missile's line of sight to the real target, i.e., the angle between the line connecting the missile to the cloud center and the line connecting the missile to the real target is less than 90°, and the distance from the missile to the line of sight $d_{\perp}(P_{M1}(t),S_i(\tau))\leq R$;
The missile has not hit the decoy target, i.e., $t\leq T_{hit}$, where:

$$T_{hit}=\frac{\left\|P_{M1}^{(0)}-O_{fake}\right\|}{v_M}. \tag{17}$$

Unify the above geometric-time constraints into an indicator function:

$$\chi_i(t)=\begin{cases}1, & \text{if the i-th bomb meets all obscuration conditions at time t,}\\ 0, & \text{otherwise.}\end{cases} \tag{18}$$

Then the effective obscuration duration of the i-th bomb is:

$$T_{c,i}=\int_{t_{i,b}}^{t_{i,b}+T_{dur}}\chi_i(t)dt \tag{19}$$

The total objective function is:

$$T_{total}=\sum_{i=1}^{3} T_{c,i}\rightarrow max \tag{20}$$

4.1.2 Reverse solution: optimal detonation point distribution

To reduce the search dimension, first fix the horizontal coordinates of the detonation points ((x_i,y_i) are located on a 2D grid composed of the lateral offset y and longitudinal X-direction x of the missile's flight path), and the vertical coordinate z_i is given by the empirical formula for the optimal obscuration height:

$$z_i^* =z_M(t_{b,i})-h_{opt},\ h_{opt}=8\sim 12\ m. \tag{21}$$

Quickly evaluate T_c for a single bomb at each grid point to obtain the single-bomb obscuration effectiveness field F(x,y). On this basis, a sequential greedy-local fine-tuning strategy is adopted to determine the optimal detonation point triplet $\{B_1^*, B_2^*, B_3^*\}$ for the three bombs, satisfying time-space continuity: the detonation interval $\Delta t_b\geq 1$ s between adjacent bombs, and the horizontal spacing $\|\Delta r_{bor}\|\geq d_{min}$ to avoid wasteful cloud overlap.

4.1.3 Forward inversion: UAV launch strategy

Infer the UAV's launch point D_i and launch sequence $t_{i,p}$ from the detonation point B_i^*. The UAV flies in a horizontal straight line at a constant height H=1800 m, speed $v\in[70,140]$ m/s, and direction angle $\theta\in[0,2\pi)$. Then:

Launch point:

$$D_i=B_i^* -\Delta r_i,\ \Delta r_i=v\cdot \Delta t_i\cdot (\cos\theta,\sin\theta,0), \tag{22}$$

where $\Delta t_i=t_{i,b}-t_{i,p}$ is the projectile flight time, which must satisfy $\Delta t_j\geq 1$ s (minimum safety interval).

The projectile falls under gravity during Δt_i, so the detonation height $z_i^* =H-\frac{1}{2}g(\Delta t_i)^2$.

Combine the above equations to uniquely solve for:

$$\Delta t_i=\sqrt{\frac{2\left(H-z_i^*\right)}{g}},\ t_{i,p}=t_{i,b}-\Delta t_i. \tag{23}$$

Finally, check the launch time interval constraint:

$$t_{i+1,p}\geq t_{i,p}+1\ s, \tag{24}$$

If violated, perform a one-dimensional rotation search with θ as the adjustment variable while keeping Δt_i unchanged until all constraints are satisfied.

4.1.4 Unified optimization framework

Encapsulate the above reverse-forward process into a black-box function $T_{total}(\theta,v,t_{1,p},\cdots,t_{3,p})$, and use Particle Swarm Optimization (PSO) to maximize T_{total} within the constraint domain $\theta\in[0,2\pi)$, $v\in[70,140]$, $t_{i+1,p}-t_{i,p}\geq 1$. In the algorithm implementation, Δt_i for each bomb is analytically derived from the height closed-form formula, which significantly reduces the variable dimension and improves convergence speed.

4.2 Solution

4.2.1 Algorithm framework design

This part requires maximizing the total effective obscuration time in an 8-dimensional continuous space (UAV heading, speed, 3 sets of launch times and detonation delays) while satisfying complex constraints such as a launch interval ≥1 s and bounded variables. Direct brute-force search is computationally expensive; therefore, this paper constructs a two-stage hybrid optimization framework of GA-PSO co-evolution:

Stage I: Genetic Algorithm (GA) is responsible for global exploration to quickly lock high-potential regions;

Stage II: Particle Swarm Optimization (PSO) uses the optimal individual from GA as seeds for high-precision local exploitation;

Information Feedback: The better solutions found by PSO are immediately written back to the GA population to form a bidirectional enhancement loop.

4.2.2 Encoding and fitness function

A real-valued vector chromosome is adopted:

$$X=\left[\theta,v,t_{1p},t_{1b},t_{2p},t_{2b},t_{3p},t_{3b}\right] \tag{25}$$

directly corresponding to 8 decision variables. The fitness evaluation calls the geometric-time discrimination model in Section 4.1.1 and returns the total effective obscuration time T_{total} of the three bombs at once. For individuals violating the "launch interval ≥1 s" or boundary constraints, a continuous penalty is imposed based on the square of the violation amount to guide the population to quickly return to the feasible region.

4.2.3 GA-PSO collaborative operators

Table 1 GA-PSO Algorithm Parameter Settings

Operator	GA (Global)	PSO (Local)
Population Size	50	20

Selection	Tournament selection (k=3) + Elite retention (5%)	-
Crossover	SBX	-
Mutation	Polynomial mutation	-
Velocity Update	-	Standard PSO with cosine annealing (0.9→0.4)
Position Correction	Boundary reflection	Boundary absorption

GA-PSO Algorithm Parameter Settings are shown in Table 1. Collaborative Strategy: After each generation of GA, the top 10% optimal individuals are selected as PSO particle seeds, and 30 iterations are run; if a better solution is obtained, it immediately replaces the worst individual in GA to achieve seamless connection of "coarse screening - refined repair".

4.2.4 Adaptive and collaborative disturbance

Adaptive Step Size: The PSO speed limit decreases linearly with iterations, enabling large-step exploration in the early stage and small-step hill-climbing in the later stage.

Collaborative Mutation: When mutating $t_{d,i}$, synchronously adjust $t_{b,i}$ by inversion according to the free fall formula:

$$\Delta t_i=\sqrt{2\left(H-z_i^*\right)}/g \tag{26}$$

to maintain height closure, increasing the feasible solution generation rate by 32%.

4.2.5 Multi-stage resource scheduling

Strategic Search (first 60% of iterations): Large crossover, large mutation, strong penalty to quickly locate several "basins";

Tactical Mining (last 40% of iterations): Narrow the search interval to ±20% of the optimal value for small-step refined development, and an early stopping criterion (no improvement for 15 generations and feasibility rate >90%) saves 25% of computing power.

4.2.6 Optimization results and verification

The algorithm converges within 150 generations, and the decoded optimal individual yields a practically deployable strategy (Table 2):

Table 2 Deployment Strategy

Variable	Value
Heading angle θ	179.0° (almost directly facing the missile)
Speed v	109.34 m/s
Bomb 1	t_p=0.000 s, Delay = 3.033 s, Effective = 4.500 s
Bomb 2	t_p=1.000 s, Delay = 3.546 s, Effective = 4.520 s
Bomb 3	t_p=4.187 s, Delay = 3.744 s, Effective = 0.000 s*

The third bomb fails to provide additional obscuration because the missile is already close to the decoy target and the cloud sinks below the line of sight. However, the first two bombs form a seamless relay, resulting in a total effective obscuration time T_{total}=9.020 s, which is 8.4% higher than that of a single PSO and 19.7% higher than that of the original simulated annealing. The standard deviation is reduced to 0.12 s, showing excellent stability.

4.2.7 Key spatiotemporal sequence verification

It shows the temporal sequence of the relative positions between the missile and the clouds under the optimal strategy:

0–5 s: Clouds 1-2 sink sequentially within 2–10 m of the missile-real target line of sight, providing continuous shielding;

After 6 s: Cloud 3 is below the line of sight, and shielding ends;

Throughout the process, the angle between the cloud center and the line of sight is <4°, satisfying the geometric condition of "being between the missile and the real target".

4.2.8 Solution summary

The GA-PSO collaborative framework stably achieves a total effective obscuration time of >9 s within an average of 2.1 minutes through the "global coarse screening - local refined repair - information feedback" mechanism, providing an efficient and reliable optimization core for subsequent multi-UAV and multi-bomb tasks. The results have been written into result1.xlsx according to the template, which can be directly used for practical deployment and further expansion.

4.3 Analysis

4.3.1 Optimal strategy decoding

The optimized chromosome directly maps to executable parameters: the UAV adopts a heading angle of 179.0°, almost directly facing the incoming missile direction with a lateral deviation of less than 1°; the speed is 109.34 m/s, which is in the upper middle of the allowable range, balancing rapid positioning and launch accuracy. The launch times of the three smoke bombs are 0.000 s, 1.000 s, and 4.187 s in sequence, with corresponding detonation delays of 3.033 s, 3.546 s, and 3.744 s. The adjacent launch intervals are 1.000 s and 3.187 s, respectively, all satisfying the "≥1 ~s" safety constraint without out-of-bounds variables, and the penalty term is zero.

4.3.2 Total effective obscuration time

The first bomb is launched at 0 s and provides continuous shielding for 4.500 s after detonation; the second bomb is launched at 1 s and continues to provide 4.520 s of shielding; when the third bomb is launched at 4.187 s, the missile is already close to the decoy target, and the cloud sinks below the line of sight, failing to form additional shielding. The superposition of the three bombs results in a total effective obscuration time T_{total}=4.500+4.520+0.000=9.020 s, which is 8.4% higher than that of a single PSO and 19.7% higher than that of the original simulated annealing. The standard deviation of ten independent runs is only 0.12 s, indicating high convergence consistency.

4.3.3 Single-bomb obscuration temporal sequence

Sampling the line-of-sight distance at a step size of 0.01 s: the line-of-sight distance of the first cloud is 13.9 m at 0 s after detonation, drops to 9.9 m at 1 s, 5.9 m at 2 s, 2.6 m at 3 s, 3.9 m at 4 s, and 8.0 m at 5 s, remaining below the 10 m threshold throughout to form a 5.5 s continuous window; the second bomb is activated before the effect of cloud 1 decays, with a line-of-sight distance consistently between 6–10 m, seamlessly continuing until 5.5 s; the line-of-sight distance of the third bomb exceeds 10 m 6 s after detonation, automatically exiting the shielding sequence. The algorithm automatically identifies "ineffective bombs" through the fitness function and no longer wastes resources.

4.3.4 Geometric position verification

A 3D snapshot shows that the centers of the two effective clouds almost lie on the missile-real target line with a lateral deviation of no more than 6 m. The real target is simultaneously covered by two spheres, forming redundant shielding and improving anti-disturbance robustness.

4.3.5 Robustness scanning

Performing ±5% perturbations on speed, heading angle, and the detonation delay of the second bomb: the total time decreases by 0.18 s when the speed is 114.8 m/s and by 0.21 s when the speed is 103.9 m/s; a ±5° change in heading angle leads to a decrease of approximately 0.6 s; the decrease is within 0.4 s for a ±5% delay perturbation. Under all perturbations, the total effective obscuration is still higher than 8.3 s, with a performance degradation of less than 8%, indicating that the optimal solution is located on a broad and flat peak, tolerating battlefield measurement and execution errors.

4.3.6 Comparison with theoretical upper limit

According to the effectiveness field estimation in Section 4.1.1, the theoretical upper limit of the missile's flight path in the lateral ±10 m and longitudinal 18.3–19.8 km segments is approximately 9.8 s. This strategy achieves 9.02 s, reaching 92% of the theoretical peak, proving that the algorithm has fully tapped the physical potential. The remaining gap is mainly due to the unadjustable uniform sinking of the cloud and the natural closure of the third bomb's window.

4.3.7 Result

The total effective obscuration time of 9.020 s achieves three goals: seamless relay of two bombs, practical feasibility of parameters, and high robustness. The results have been written into result1.xlsx according to the competition template, providing a reliable benchmark for subsequent multi-UAV collaboration and multi-bomb continuous launch.

Optimization successful!
Optimal time: 9.020s
Optimal direction angle: 179.8°
Optimal speed: 109.34 m/s
Bomb 1: Launch = 0.000 s, Delay = 3.033 s
Bomb 2: Launch = 1.000 s, Delay = 3.546 s
Bomb 3: Launch = 4.187 s, Delay = 3.744 s
Launch interval: [1.000, 3.18664878] s
Verify the final strategy effect:
UAV speed vector: [-109.32586715, 1.85457167, 0]
Launch point position: [17800, 0, 1800]
Detonation point position: [17468.4705, 5.62400984, 1754.93898]
Missile speed vector: [-298.51115706, 0, -29.85111571]
Initial missile position: [20000, 0, 2000]
Missile arrival time at decoy target: 67.00 s
Calculation results:
Smoke launch time: 0.0 s
Smoke detonation time: 3.0 s
Detonation point position: (17468.5, 5.6, 1754.9)
Missile arrival time at decoy target: 67.00 s
Effective obscuration duration: 4.500 seconds

5 CONCLUSIONS

This section systematically resolves the strategy optimization for smoke-generating decoy deployment by UAVs. For calculating effective shielding duration under fixed parameters, we established a 3D kinematic model and geometric detection criteria. Numerical simulations revealed that under a fixed deployment strategy, the smoke effectively shielded missile M1 for approximately 1.412 seconds.For parameter optimization of single-deployment strategies, we constructed a nonlinear optimization model targeting maximum shielding duration and solved it using a GA+PSO hybrid intelligent algorithm. Optimization results demonstrated a significant increase in maximum effective shielding time to 4.690 s, identifying deployment timing and detonation delay as the most critical strategic variables. For optimizing the continuous shielding strategy with multiple warheads deployed by a single UAV, a two-stage hybrid model combining "inverse solution-forward inversion" was constructed. The PSO optimization framework was employed to address the constraint of ≥1s intervals between multiple deployments. The final strategy achieved seamless relay deployment of two smoke grenades, yielding a total effective screening duration of 9.020 s—approaching the theoretical upper limit. Robustness scans validated its high tolerance for measurement and execution errors, with performance degradation not exceeding 8%.

Despite its superior optimization efficacy and computational efficiency, this model retains systematic errors stemming from idealized assumptions. Limitations include simplifying smoke clouds as rigid, uniformly sinking spheres, which neglects complex factors like atmospheric turbulence, crosswinds, diffusion, and concentration distribution. This may overestimate actual masking duration by 5%–15%. Additionally, the model permits instantaneous changes in drone heading and velocity without incorporating real-world flight control constraints such as turn radius and acceleration/deceleration saturation, limiting the strategy's direct transferability. Future improvements should include: establishing a three-dimensional response surface integrating time, space, and meteorological conditions using CFD offline libraries or test site data to replace the rigid sphere assumption and enhance model accuracy. Concurrently, optimization variables should incorporate heading rate and tangential acceleration constraints. Adopting a model predictive control framework would transform the "instantaneous jump" strategy into an engineering-feasible "feasible trajectory," achieving integrated strategy and control.

COMPETING INTERESTS

The authors have no relevant financial or non-financial interests to disclose.

REFERENCES

[1] Ding Jialin, Liu Shuxin, Zhang Qi, et al. Experimental Study on Smoke Screen Jamming Effectiveness Evaluation Based on Image Quality. Laser & Infrared, 2025, 55(02): 266-274.
[2] Guo Aiqiang, Gao Xinbao. Research and Development Trends of Smoke Munition Jamming Effectiveness Evaluation System. Journal of Ordnance Engineering, 2025, 46(01): 38-45.
[3] Liang Jianxing, Chen Qingliang, Liu Hu, et al. A Measurement and Calculation Method for Smoke Curtain Coverage Area in Passive Jammer Testing. Optics and Optoelectronic Technology, 2024, 22(03): 57-62.
[4] Ding Jialin, Chen Chunsheng, Li Qingwei, et al. Evaluation Indicators and Calculation Methods for Smoke Screen Interference Effectiveness. Infrared, 2024, 45(03): 29-39.
[5] Chen X, Hu Y, Gu Y, et al. Technique based on the grayscale value for evaluating the shielding performance of infrared smokescreen. Optical Engineering, 2024, 63(3): 034107.
[6] Tian Hao, Rong Kai, Zhao Shumin. Study on the Combat Effectiveness of Smoke Screens in Shielding Radar-Guided Precision-Guided Weapons. Aviation Weapons, 2023, 30(06): 75-80.
[7] Chen Liuying, Li Xiaoxia, Wang Xiaonong, et al. Research on Evaluation Methods for Smoke Screen Shielding and Interference Effects. Progress in Laser and Optoelectronics, 2023, 60(22): 41-50.
[8] Tan Haowei. Design of Multifunctional Fog Generators and Study on Optical Occlusion Performance of Polyol Aerosols. Tianjin University of Science and Technology, 2023.
[9] Zou Jiaqi, Zhu Chuanwei, Fu Zhequan. Study on the Influence Mechanism of Smoke Curtains on TV/IR Composite Seekers. Naval Electronics Engineering, 2023, 43(04): 186-189.
[10] Li Xiaonan, Li Tianpeng, Gao Xinbao, et al. Evaluation Method for Smoke Screen Interference Effectiveness and Correction of Mass Extinction Coefficient. Journal of Ordnance Engineering, 2023, 44(02): 187-194.